Development of an electrochemical fabrication method of Au tips for STM studies

(STM 研究のための金探針の電気化学的作製法の開発)

Department of Materials Science

Graduate School of Science and Engineering

Saitama University

Bo Yang

埼玉大学大学院　理工学研究科　物質科学専攻

楊　波

Dissertation

Development of an electrochemical fabrication method of Au tips for STM studies
(STM 研究のための金探針の電気化学的作製法の開発)

A Dissertation Submitted to Saitama University

for the Degree of Doctor of Science

Bo Yang

Department of Materials Science

Graduate School of Science and Engineering

Saitama University

Supervised by Professor Yousoo Kim

Chapter 1

General introduction

This doctoral dissertation is organized as follows: Chapter 1 provides a general introduction to Au tips, Au(111) surfaces, dimethyl disulfide and interactions at molecular level. The methodologies used in the following chapters are introduced in Chapter 2. Chapter 3 and 4 present fabrication of Au tips by three-electrode electrochemical etching method and STM investigation of the dissociation of a single $(CH_3S)_2$ molecule on the Au(111) surface, respectively. Finally, conclusions and further perspectives are summarized in Chapter 5.

1.1 Outline of the thesis

The general introduction and background of this doctoral thesis are summarized in Chapter 1. This doctoral studies mainly include my personal motivation and interests in electrochemical fabrication of Au tips and dissociation of a single molecule on noble metal substrate. Basic information regarding Au tips, Au(111) surfaces, dimethyl disulfide, and interactions at molecular level is introduced in sections 1.2, 1.3, 1.4, and 1.5, respectively.

Chapter 2 is an introduction of the methodologies used in my doctoral study. Section 2.1 focuses on the electrochemical etching in fabricating Au tips and the key factors including applied potentials, an electrolyte, electrode system and other parameters. Section 2.2 moves to a scanning tunneling microscope (STM). This part mainly includes the basic theory and working principle of the STM and its instrumentation.

Chapter 3 describes the fabrication of sharp Au tips by three-electrode electrochemical etching with high reproducibility and controllability. Gold (Au) tips have wide applications in local spectroscopies such as tip enhanced Raman spectroscopy (TERS) because of not only high chemical stability but also strong localized surface plasmon resonance (LSPR) in the visible and near-infrared regions.[1-3] The LSPR strongly depends on the tip shape.[4-6] However, the conventional fabrication method of the Au tips by electrochemical etching with two electrodes has the problems about both controllability and reproducibility of the tip shape. Here, we apply a three-electrode electrochemical method to fabrication of the Au tips. Tip sharpness is well controlled by the applied potential with high reproducibility.

Chapter 4 describes the studies of single-molecule reactions on surfaces using the STM, which provides unprecedented insight into the structure of reactants and products, as well as the reaction pathways.[2,7-9] Photo-induced dissociation is one of the important applications of solar energy, a clean and renewable energy resource. However, this reaction is not feasible for small molecules in the gas and liquid phases, because there is wide energy gap between the frontier molecular orbitals such as the highest occupied molecular orbital (HOMO) and the lowest unoccupied molecular orbital (LUMO).[10] Molecular adsorption on solid surfaces provides a new opportunity for photochemical reactions with visible light, based on the reconstruction of interfacial electronic structures due to the molecule-surface interaction. Particularly, the LUMO-derived MOs overlap with the metal surface and so lifetime of the photo-excited state becomes long enough to induce dissociation.[10] Recently, plasmon-induced dissociation of a single DMDS molecule on Ag(111) surface with a Ag tip has been realized.[11] How about the case of the molecules adsorbed on Au(111) with a Au tip? Therefore we carried out the same trial of the same molecule with

a 670 nm-visible light. Dissociation reaction occurred under the excitation of plasmon. Any molecular motion such as rotation, translation and desorption was not observed.

Previous STM studies revealed the tunneling electron-induced dissociation of adsorbed molecules on noble metal surfaces.[12-14] As for a single DMDS molecule, dissociation reactions occurred on Au(111) surface with a W tip.[15] However, recent study found both dissociation and rotation reactions occurred on Ag(111) surface with the W tip.[11] We further investigated the case of Au(111) substrate with the W tip and three reaction were found: dissociation, rotation and desorption.

1.2 Au tips

Without a tip, the STM can't work normally. The production of tunneling current depends on the interaction between tip and sample. What's more, the acquisition of STM data is closely related to tip's bias and position. Figure 1.1 shows the working principle of the STM.

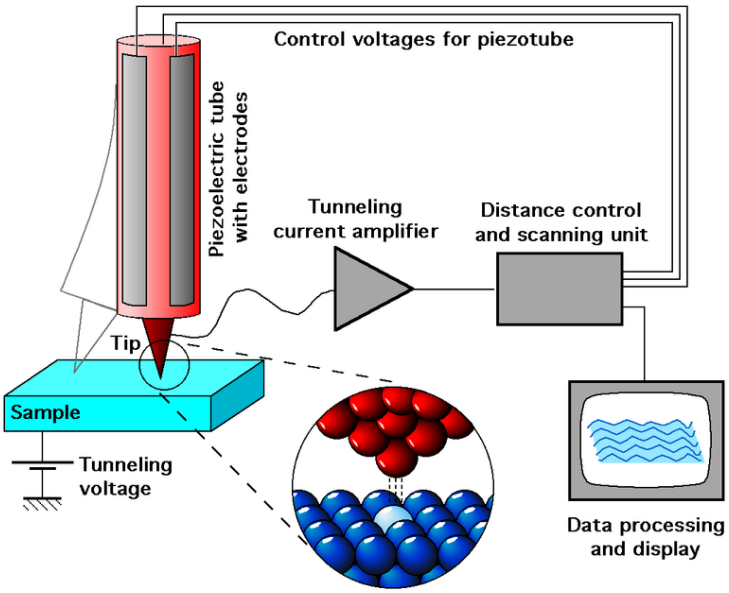

Figure 1.1. A diagram of the working principle of a STM (http://en.wikipedia.org).

As mentioned in Part 1.1, Au has both strong LSPR effect and high chemical stability, making it an excellent candidate to fabricate STM tips. In addition, the Au tips also have wide applications in (other) local spectroscopies (Figure 1.2).

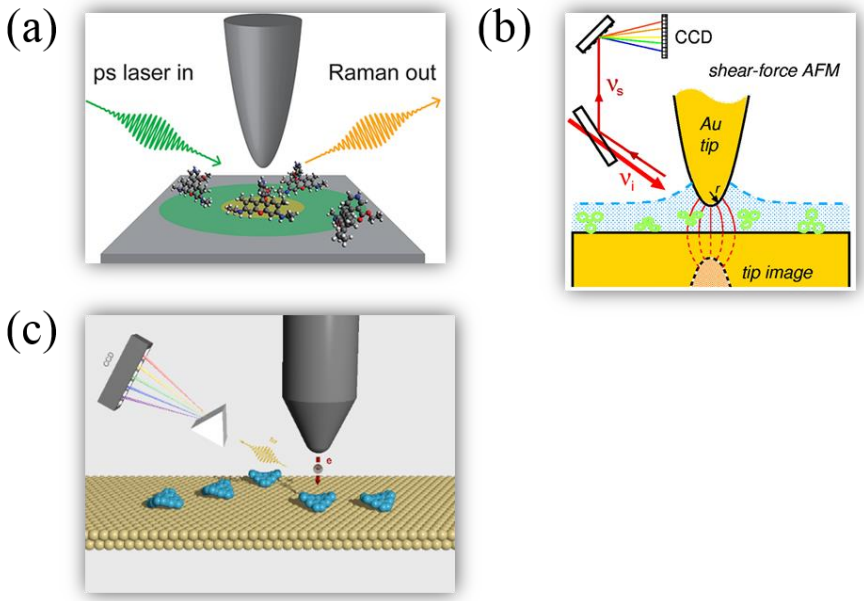

Figure 1.2. Examples of the applications of Au tips: (a) tip-enhanced Raman spectroscopy (http://chemgroups.northwestern.edu), (b) shear-force atomic force microscopy (http://nano-optics.colorado.edu), and (c) light emission/luminescence (http://www.int.kit.edu).

1.3 Au(111) surfaces

To modify chemical bonds bonding in surface science applications, one requires a relatively chemically inert surface to which large molecules adhere primarily through noncovalent van der Waals interactions, yet one that is reactive enough to cleave only a

few bonds.[16] Au(111) has technical advantages in that it is relatively easy to obtain a clean atomically flat surface (Figure 1.3).[17]

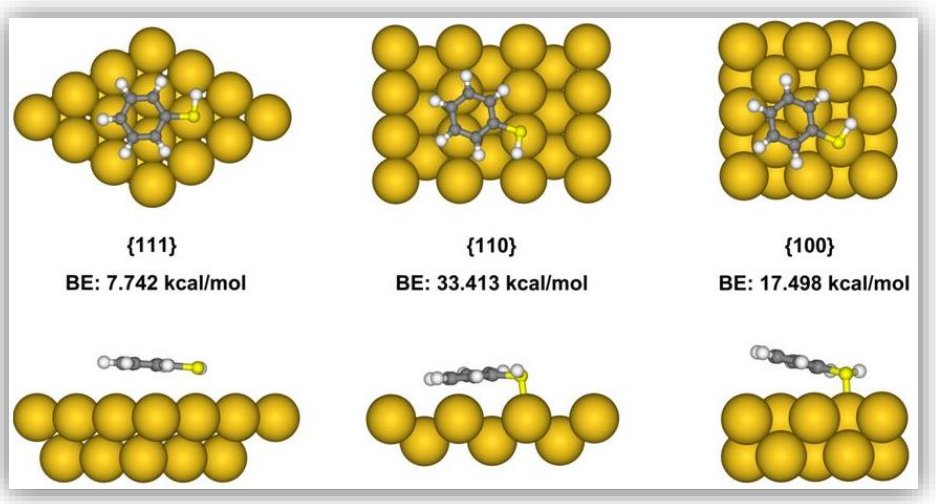

Figure 1.3. Top and side views of the most stable structures of thiophenol on Au{111}, {110}, and {100} surfaces. BE denotes binding energy. Reproduced with permission from ref. 17.

Its unique reconstruction has been characterized experimentally using the STM[18-22] and other surface science techniques,[23-26] and a large number of molecular assembly studies have been performed on this surface.[27-34] Figure 1.4 indicates the formation and a typical STM images of the √3×22 reconstruction on Au(111).[35,36]

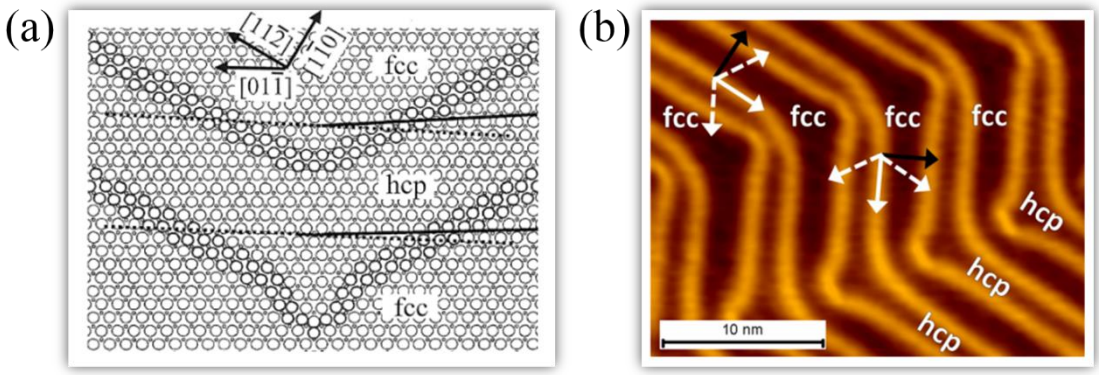

Figure 1.4. Formation and a typical STM images of the √3×22 reconstruction on Au(111) surface. Reproduced with permission from ref. 35 and ref. 36, respectively.

The renewed interest in the chemical reactivity on the Au(111) surface is intricately linked to its atomic-level surface structure and its reconstruction, and provides a significant challenge to modern electronic structure theory. In fact, most density functional computational studies make the approximation that Au(111) is an infinite, perfect, atomically flat close-packed face-centered-cubic (fcc) surface.

1.4 Dimethyl disulfide

Dimethyl disulfide (DMDS) is an organic chemical compound with the molecular formula CH_3SSCH_3 which is the simplest disulfide. The systematic IUPAC name is 2-sulfide, 2-methyl. It is a symmetrically structural substance, divided by the S-S chemical bond. Below show the molecular formula and three-dimensional model, respectively.

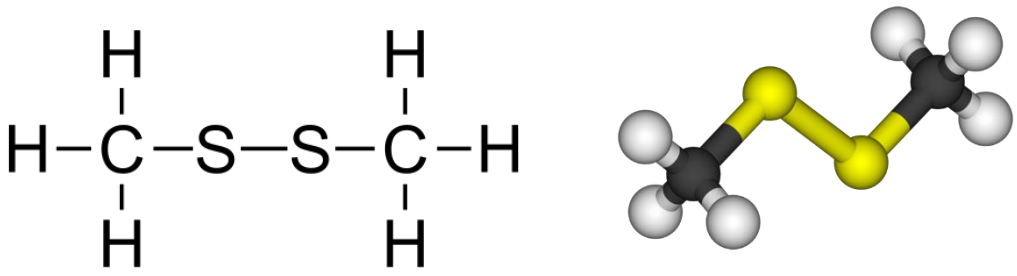

Figure 1.5. Molecular formula and three-dimensional model of a single $(CH_3S)_2$ molecule.

From the previous work,[37] the adsorbed $(CH_3S)_2$ molecule has two conformations on Au(111) substrate: *cis*- and *trans*- symmetry (Figure 1.6). The S-S bond is aligned with the close-packed direction on the Au(111) surface and is located above the Au-Au bridge

site.

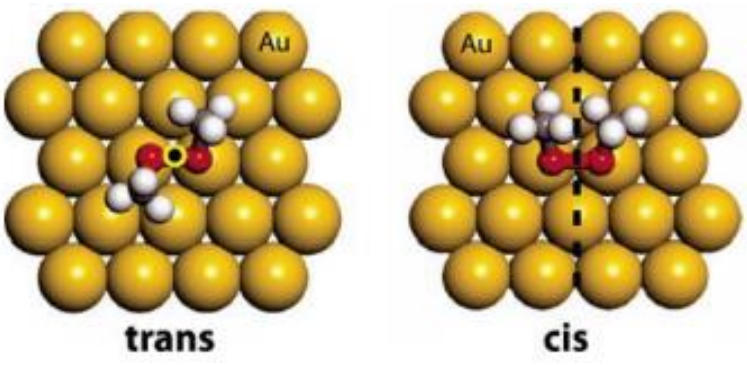

Figure 1.6. *cis*- and *trans*- symmetry of the $(CH_3S)_2$ molecule on Au(111) substrate. The red line marks the direction of the S-S bond. Reproduced with permission from ref. 37.

1.5 Interactions at molecular level

1.5.1 Intermolecular interactions

Chemical bonds can be classified as strong and weak forces. Strong forces include ionic, covalent and metallic bonding. Ionic and covalent bonds form inorganic salts, while determining their structures and properties. Metallic bonding forms a metal crystal in which electrons are delocalized, resulting in conductive properties.

"Chemical structure" refers to the arrangement of atoms in one molecule, in other words, it is a model regarding bond distances and angles between linked atoms. However, the molecular conformation can be changed by temperature or solvent in spite of the same "chemical structure". This originates from the weak forces between atoms or groups, called intermolecular interactions.

Although intermolecular interactions are *ca.* 1-3 orders of magnitude lower than covalent bonds in energy, no molecule could maintain a liquid or solid phase if there's no interaction between atoms or groups.

1.5.2 Intramolecular interactions

An intramolecular force can hold together the atoms making up a molecule or compound.[38] It includes all types of chemical bonds. Usually, they are stronger than intermolecular forces which present between atoms or molecules that are not bonded. As mentioned above, the classical model mainly identifies three kinds of chemical bonds: ionic, covalent and metallic. They distinguish with each other by the degree of charge separation between participating atoms.[39] In addition, their bond enthalpies are also different, thus affect the physical and chemical properties of the according molecule.

An ionic bond involves a complete transfer of one or more valence electrons of atoms participating in bond formation, resulting in a positive ion and a negative ion bound together by electrostatic forces.[40] Electrons in an ionic bond tend to be mostly found around one of the two constituent atoms due to the large electronegativity difference between the two atoms; this is often described as one atom giving electrons to the other. This type of bond is generally formed between a metal and nonmetal, such as sodium and chlorine in NaCl. Sodium would give an electron to chlorine, forming a positively charged sodium ion and a negatively charged chlorine ion.

In a covalent bond, the electrons are shared evenly between the two atoms and there is little or no charge separation. Covalent bonds are generally formed between two nonmetals. There are several types of covalent bonds: in polar covalent bonds, electrons are more likely to be found around one of the two atoms, whereas in nonpolar covalent bonds, electrons are evenly shared. Homonuclear diatomic molecules are purely covalent. The polarity of a covalent bond is determined by the electronegativity of each atom and thus a polar covalent bond has a dipole moment pointing from the partial positive end to the

partial negative end. Polar covalent bonds represent an intermediate type in which the electrons are neither completely transferred from one atom to another nor evenly shared.

1.5.3 Interactions between molecules and the metal surface

In general, the surface charge distribution of an organic molecule varies when it is deposited on a metal surface, resulting in an electronic double layer (EDL) at the interface (Figure 1.7). The formation of EDL depends on several factors: (1) Charge transfer between the molecule and metal, (2) chemical bonding, (3) bias of electron cloud, (4) push back.[41] The molecule is physically adsorbed on the metal surface by van der Waals interactions.

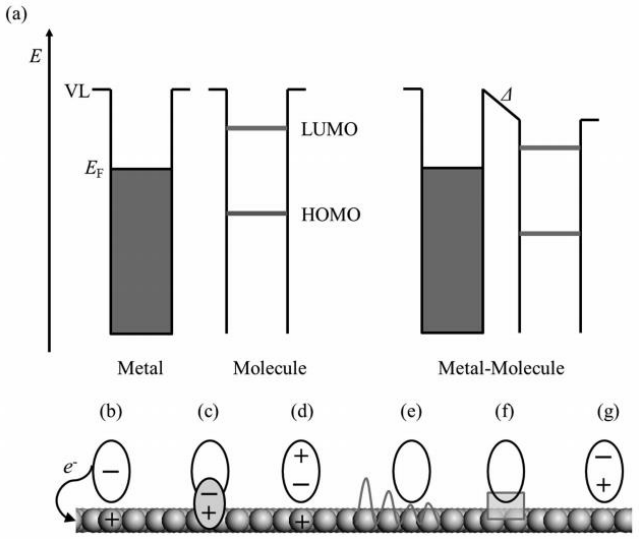

Figure 1.7. Formation and possible origin of electrical dipole layer at metal-molecule interface. Reproduced with permission from ref. 41.

1.6 References

1. Tsai, C.-S.; Wang, J.-K.; Skodje, R. T.; Lin, J.-C. *J. Am. Chem. Soc.* **2005**, *127*, 10788.

2. Hossain, Md. Z.; Kato, H. S.; Kawai, M. *J. Am. Chem. Soc.* **2005**, *127*, 15030.

3. Henzl, J.; Mehlhorn, M.; Gawronski, H.; Rieder, K.-H.; Morgenstern, K. *Angew. Chem., Int. Ed*. **2006**, *45*, 603.

4. Ho, W. *J. Chem. Phys.* **2002**, *117*, 11033.

5. Lu, P. H.; Polanyi, J. C.; Rogers, D. *J. Chem. Phys.* **1999**, *111*, 9905.

6. Sloan, P. A.; Palmer, R. E. *Nature* **2005**, *434*, 367.

7. Maksymovych, P.; Sorescu, D. C.; Yates, J. T., Jr. *J. Phys. Chem. B* **2006**, *110*, 21161.

8. Hossain, Md. Z.; Kato, H. S.; Kawai, M. *J. Am. Chem. Soc.* **2005**, *127*, 15030.

9. Lastapis, M.; Martin, M.; Riedel, D.; Hellner, L.; Comtet, G.; Dujardin, G. *Science* **2005**, *308*, 1000.

10. Kazuma, E.; Jung, J.; Ueba, H.; Trenary, M.; Kim, Y. *J. Am. Chem. Soc*. **2017**, *139*, 3115.

11. 36. Kazuma, E.; Jung, J.; Ueba, H.; Trenary, M.; Kim, Y. *Science* **2018**, *360*, 521.

12. Ho, W. *J. Chem. Phys.* **2002**, *117*, 11033.

13. Lu, P. H.; Polanyi, J. C.; Rogers, D. *J. Chem. Phys.* **1999**, *111*, 9905.

14. Sloan, P. A.; Palmer, R. E. *Nature* **2005**, *434*, 367.

15. Peter, M.; John T. Y. *J. Am. Chem. Soc.* **2006**, *128*, 10642.

16. Hanke, F.; Bjork, J. *Phys. Rev. B* **2013**, *87*, 235422.

17. Wu, H.-L.; Tsai, H.-R.; Hung,Y.-T.; Lao, K.-U.; Liao, C.-W.; Chung, P.-J.; Huang, J.-S.; Chen, I.-C.; Huang, M. H. *Inorg. Chem.* **2011**, *50*, 8106.

18. Jaklevic, R. C.; Elie, L. *Phys. Rev. Lett.* **1988**, *60*, 120.

19. Dovek, M. M.; Lang, C. A.; Nogami, J.; Quate, C. F. *Phys. Rev. B* **1989**, *40*, 11973.

20. Barth, J. V.; Brune, H.; Ertl, G.; Behm, R. J. *Phys. Rev. B* **1990**, *42*, 9307.

21. Hasegawa, Y.; Avouris, P. *Science* **1992**, *258*, 1763.

22. Nie, H. Y.; Mizutani, W.; Tokumoto, H. *Surf. Sci.* **1994**, *311*, L649.

23. Van Hove, M. A.; Koestner, R. J.; Stair, P. C.; Biberian, J. P.; Kesmodel, L. L.; Bartos, I.; Somorjai, G. A. *Surf. Sci.* **1981**, *103*, 189.

24. Harten, U.; Lahee, A. M.; Toennies, J. P.; Woll, C. *Phys. Rev. Lett.* **1985**, *54*, 2619.

25. Huang, K. G.; Gibbs, D.; Zehner, D. M.; Sandy, A. R.; Mochrie, S. G. J. *Phys. Rev. Lett.* **1990**, *65*, 3313.

26. Sandy, A. R.; Mochrie, S. G. J.; Zehner, D. M.; Huang, K. G.; Gibbs, D. *Phys. Rev. B* **1991**, *43*, 4667.

27. Grill, L.; Dyer, M.; Lafferentz, L.; Persson, M.; Peters, M. V.; Hecht, S. *Nat. Nanotechnol.* **2007**, *2*, 687.

28. Cai, J.; Ruffieux, P.; Jaafar, R.; Bieri, M.; Braun, T.; Blankenburg, S.; Muoth, M.; Seitsonen, A. P.; Saleh, M.; Feng, X.; Mullen, K.; Fasel, R. *Nature* **2010**, *466*, 470.

29. Tao, N. J.; DeRose, J. A.; Lindsay, S. M. *J. Phys. Chem.* **1993**, *97*, 910.

30. Yokoyama, T.; Yokoyama, S.; Kamikado, T.; Okuno, Y.; Mashiko, S. *Nature* **2001**, *413*, 619.

31. Perdigao, L. M. A.; Perkins, E. W.; Ma, J.; Staniec, P. A.; Rogers, B. L.; Champness, N. R.; Beton, P. H. *J. Phys. Chem. B* **2006**, *110*, 12539.

32. Staniec, P. A.; Perdigao, L.; Saywell, A.; Champness, N. R.; Beton, P. H. *Chem. Phys. Chem.* **2007**, *8*, 2177.

33. Lafferentz, L.; Ample, F.; Yu, H.; Hecht, S.; Joachim, C.; Grill, L. *Science* **2009**, *323*, 1193.

34. Treier, M.; Pignedoli, C.; Laino, T.; Rieger, R.; Mullen, K.; Passerone, D.; Fasel, R. *Nat. Chem.* **2010**, *3*, 61.

35. Xie, Z. X.; Xu, X.; Tang, J.; Mao, B. W. *J. Phys. Chem. B* **2000**, *104*, 11719.

36. Murphy, C. J. *et al. J. Chem. Phys.* **2015**, *142*, 101915.

37. Peter, M.; John, T. Y. *J. Am. Chem. Soc.* **2006**, *128*, 10642.

38. Zumdahl, S. S.; Zumdahl, S. A. *Houghton Mifflin.* **2007**, ISBN 0618713700.

39. Oxtoby, D. W.; Gills, H. P.; Campion, A. *Belmont, Calif.: Brooks/Cole Cengage Learning* **2012**, ISBN 978-0-8400-4931-5.

40. Bader, R. F. W.; Henneker, W. H. *J. Am. Chem. Soc.* **1965**, *87*, 3063.

41. Ueji, K. *Doctoral dissertation* **2016**, P14.

Chapter 2

Methodologies

2.1 Electrochemical etching

Several methods have been developed to fabricate Au tips over the decades, mainly including the follows: (1) electrochemical etching,[1-5] (2) chemical polishing,[6] (3) ion milling,[7] (4) cathode sputtering,[8] (5) whisker growth[9-11] and (6) mechanical shaping.[12-14] (Figure 2.1).

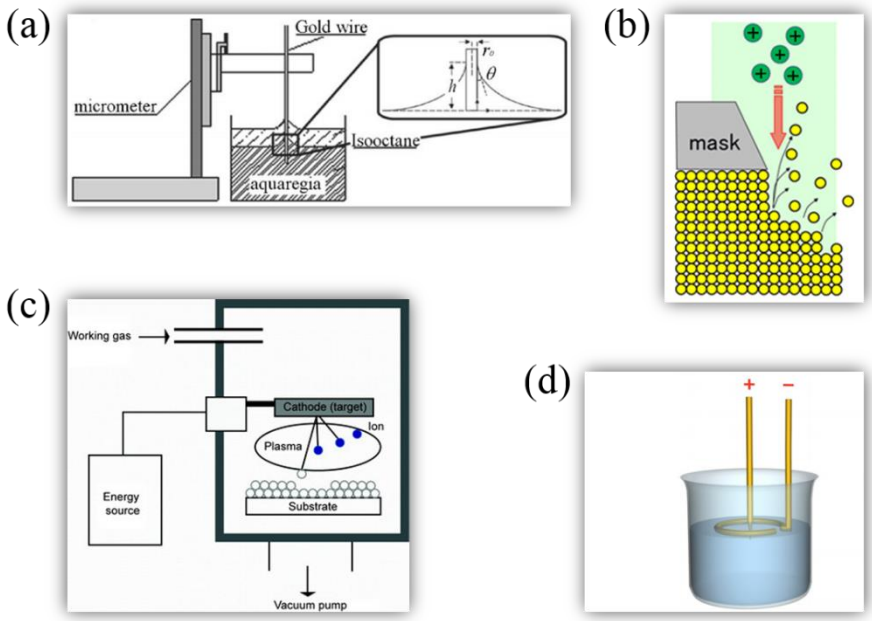

Figure 2.1. Schematics of main methods to fabricate Au tips: (a) chemical polishing,[6] (b) ion milling,[7] (c) cathode sputtering[8] and (d) electrochemical etching.[1] (a), (b), (c), and (d): Reproduced with permission from ref. 6, 7, 8 and 1, respectively.

Table 2.1. Advantages and disadvantages of the methods to fabricate Au tips.

Methods	**Advantages**	**Disadvantages**
Electrochemical etching	Easy to operate; low cost; good anticorrosion; better reproducibility and reliability	Highly polluting
Chemical polishing	Less equipment investment; rapid; high efficiency; good anticorrosion capability	Processing complexity; high rejection rate; toxicity and fire risk; equipment corrosion; expensive materials recycling
Ion milling	Extremely anisotropic; independent of material composition	Extremely high ion damage; non-selective; residue
Vapor, electron-beam deposition	Large range of deposition rate; high material utilization efficiency; structural and morphological control	Non-uniform evaporation rate; certain materials are not well-suited to evaporation by EBPVD
Mechanical shaping	Good leveling and high brightness after polishing; suitable for simple, medium and small size products	Take much labor; cause serious pollution; the luster can't be consistent and durable
Cutting	The easiest way	Multiple tips; poor reproducibility

Machining	High accuracy; no direct contact of tool and workpiece; tool life is more longer; quieter operation	High cost; complex set-up; skilled operator required

The advantages and disadvantages of these methods are summarized in Table 2.1 above. Electrochemistry is the branch of physical chemistry that studies the relationship between electricity, as a measurable and quantitative phenomenon, and identifiable chemical changes, with either electricity considered an outcome of a particular chemical change or vice-versa. These reactions involve electric charges moving between electrodes and an electrolyte (or ionic species in a solution). Thus electrochemistry deals with the interaction between electrical energy and chemical change. The electrochemical etching system includes an electrolyte, a working electrode (WE) and a counter electrode (CE). The anodic reaction $(A \rightarrow A^+ + e^-)$ and cathodic reaction $(B^+ + e^- \rightarrow B)$ occur on WE and CE, respectively.

Figure 2.2 indicates a brief flow chart of the tip fabrication process. First, the Au ring (acts as CE) is fully immersed into the electrolyte solution, and then pulled up to the interface of air and liquid to form a meniscus. Second, the Au wire (acts as WE) approaches to the surface of the electrolyte solution until they just contact. Finally, rotate the cylinder ruler for two laps to make 1 mm-immersion depth of Au wire. When the etching potential is applied, an electrochemical cell forms and the etching starts at the same time. After the potential is applied, a large number of Cl^- accumulate on the WE (Au ring). So the etching reaction ($Au + 4Cl^- \rightarrow AuCl_4^- + 3e^-$) is stronger. $U_{out} - IR = U_{interface}$. For "IR" part, the distance between CE and WE is the shortest at the CE level,

so the largest etching current produces. With approaching to the lower position, the according distance increases and etching becomes weaker and weaker.

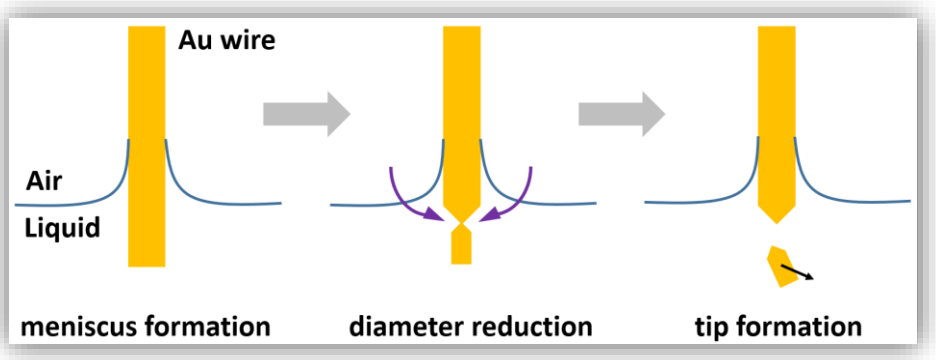

Figure 2.2. A brief flow chart of the tip fabrication process by electrochemical etching.

Figure 2.3 shows the flow directions of electrons and ions (cations and anions) in a two-electrode electrochemical system. Cations flow to cathode, mainly including Au^+ and H^+. Anions flow to anode, mainly including Cl^- and OH^-. In tip fabrication, the shape of CE is like a ring located at the interface between air and solution.

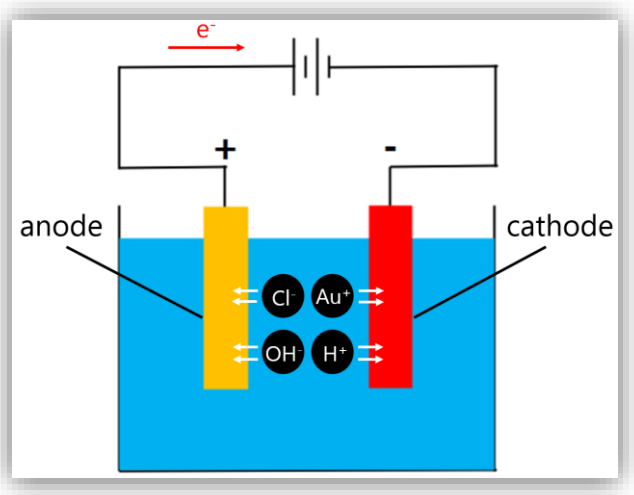

Figure 2.3. The flow directions of electrons and ions in a two-electrode electrochemical system. The electrolyte is a Cl^- contained solution.

2.2 Experimental parameters

2.2.1 Applied potential

Applied potential is one of the most important parameters to produce sharp gold tips with a smooth surface and an appropriate aspect ratio. For different etchants the optimal voltages are different. Both DC[15-19] and AC (including square DC-pulsed voltage) [19-23] voltage have been used for etching. Generally, DC etching is simple and the etching process generally finishes in minutes; whereas, the AC method can further accelerate the mass transfer process and thus the supplement of the etchants, yielding a faster etching rate[21]. For the AC method etching parameters such as high limit voltage, low limit voltage, period time, and duty cycle can also be controlled to fabricate gold tips with designed geometries[24]. What's more, the value of the etching voltage greatly affect the tip quality. Figure 2.4 shows an example of the dependence relationship between tip morphology and etching voltage[20].

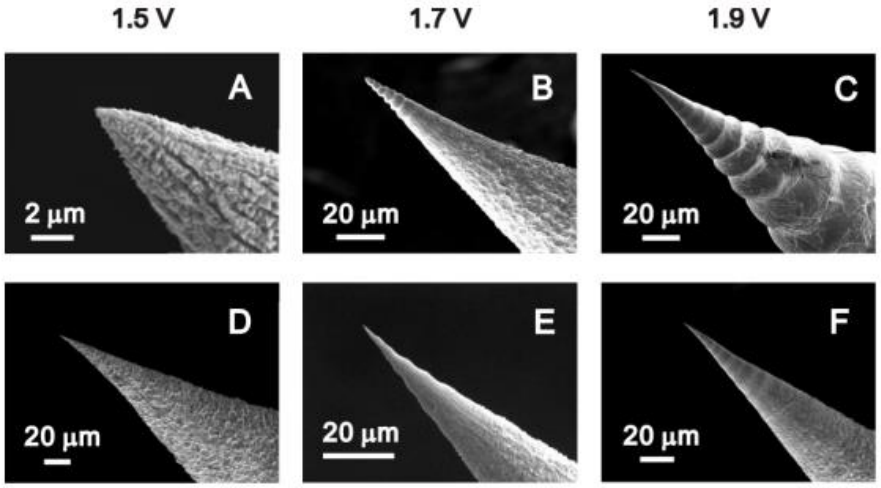

Figure 2.4. SEM images of optical tips DC electrochemically etched with both the standard (A)–(C) and modified (D)–(F) electrochemical cells at different voltages. Reproduced with permission from ref. 20.

2.2.2 Electrolyte

Electrolyte strongly affects the value of applied potential, etching time and the morphology of the tip (including the chemical and structural quality). So far, the main etchants for the fabrication of Au tips include 3 *M* NaCl, a 1:1 mixture of concentrated HCl and ethanol[15], 3 *M* NaCl and 1% $HClO_4$[22], 1 *M* HCl[25,26], and 0.8 *M* KCN[27]. Table 2.2 is a summary of the etching voltage, mean etching time, and mean radius of curvature for various etching solutions[22]. We can see that the mean radius of curvature for 3 *M* NaCl is the largest (10 μm) and the mean etching is more than 30 min. However, when 1% $HClO_4$ is mixed with the former, the etching greatly shortened to 4 min. It is surprising that the averaged radius can become 15 nm.

Table 2.2. Etching voltage, mean etching time, and mean radius of curvature for various etching solutions. Reproduced with permission from ref. 22.

Etchant	3*M* NaCl	1:1 conc. HCl/ ethanol	1*M* HCl	3*M* NaCl in 1% HCl	3*M* NaCl in 1% $HClO_4$
Etching voltage (V ac)	10	5	2.5	2.5	2.5
Mean etch time (s)	1900	350	510	320	240
Mean radius of curvature (nm)	10 000	1100	230	3600	15

To observe the morphologies more intuitively, the transmission electron microscope (TEM) images are compared (Figure 2.5). The tips fabricated by using 3.0 *M* NaCl and 3.0 *M* NaCl in 1% HCl are very rough and irregular. In comparison, the solutions of 1:1 concentrated HCl/ethanol and 1.0 *M* HCl can produce smooth and sharp tips; but both

introduce HCl, which is a strong and deleterious acid. From the reference[28], the formation of the Au oxide during etching can be expressed as:

$$Au + H_2O \leftrightarrow AuOH + H^+ + e^-$$

$$AuOH \leftrightarrow AuO + H^+ + e^-$$

If the pH is smaller (higher concentration of the proton), the etching process will be promoted and the formation of oxide be inversed.

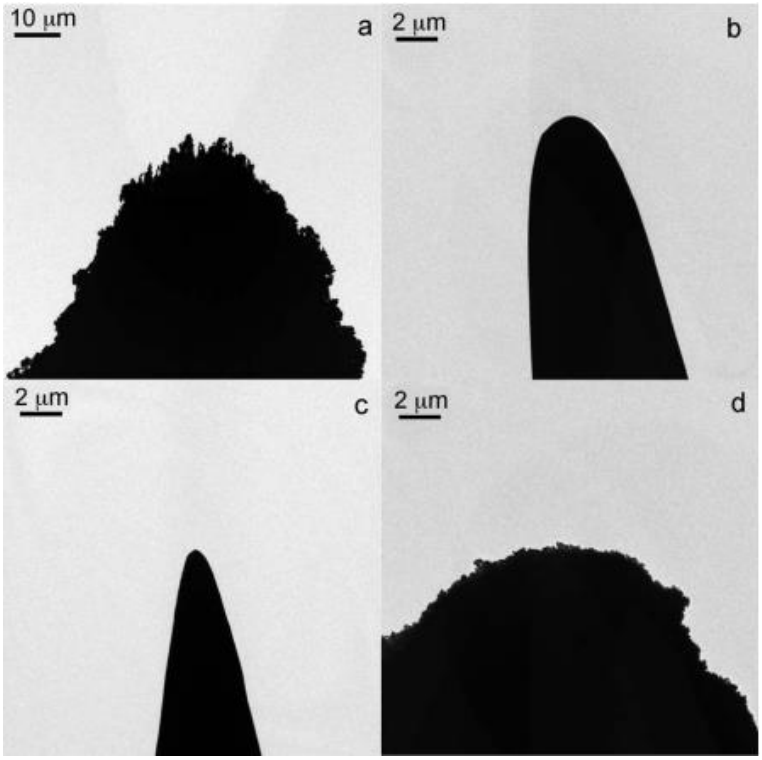

Figure 2.5 TEM images of Au tips etched in (a) 3.0 *M* NaCl, (b) 1:1 concentrated HCl/ethanol, (c) 1.0 *M* HCl, and (d) 3.0 *M* NaCl in 1% HCl. Reproduced with permission from ref. 22.

Also, the concentration of electrolyte has a large effect on tip quality. Figure 2.6 demon-

strates the field emission-scanning electron microscope (FE-SEM) images of the tips prepared from glycerol with different concentrations: (a) 0%, (b) 11%, (c) 14%, (d) 20%, and (e) 50%. Figure 2.6f is a graph of tip radius and capillary numbers versus glycerol concentrations.

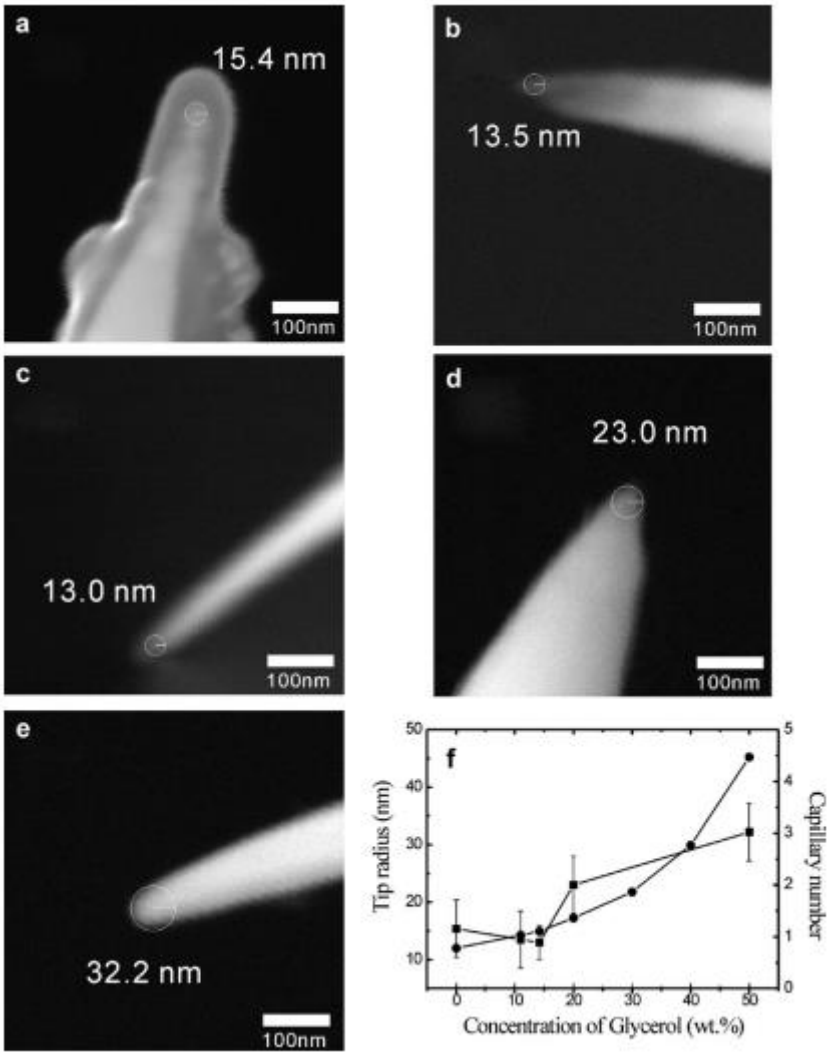

Figure 2.6. FE-SEM images of the tips whose concentration of glycerol are (a) 0%, (b) 11%, (c) 14%, (d) 20%, and (e) 50%. (f) A graph of tip radius and capillary numbers versus glycerol concentrations. Reproduced with permission from ref. 23.

2.2.3 Electrode system

All of the previous reports were based on the two-electrode electrochemical system consisting of WE and CE, seen from Table 2.2. In a real experiment, the components of the solution in an electrochemical cell is constantly changing during the etching process. So one weak point of two-electrode system is the fluctuation of the potential, which makes instability in etching condition. This will be further discussed in latter part.

2.2.4 Other parameters

The last are some not so critical parameters, such as the diameter (depends on the utility, usually 0.25 mm) and crystallinity of the Au wire, the material of counter electrode (noble metal ring), the immersion method, the number of steps, etc.[10,16]

Here we summarized the main findings of previous studies, including Au diameter, electrode system, cathode, electrolyte, experimental steps, etching voltage and apex radius (Table 2.3).

Table. 2.3. A detailed summary of the previous reports of Au tip fabrication.

Paper info.	**Au diameter**	**E-system**	**Cathode**	**Electrolyte**	**Step**	**Voltage**	**Apex radius**
Mater. Sci. Eng.: B. **2000**, *74*, 229	0.25 mm	2E	?	0.8M-97% KCN solution	Two	8, 12, 16, 20 V	200-500 nm
Anal. Chem. **2003**, *75*, 1089	0.25 mm	2E	?	3 M NaCl	Two	AC 10 V	?

Appl. Phys. Lett **2007**, *91*, 101105	0.25 mm	2E	Au ring	HCl solution	Two	2.1, 2.2, 2.4 V	?
Rev. Sci. Instrum. **2004**, *75*, 837	0.25 mm	2E	Au ring	HCl solution (+ethanol)	Two	DC 2.2-2.4 V	≤30 nm
Rev. Sci. Instrum. **2007**, *78*, 113703	0.25 mm	2E	Au ring	3M NaCl in 1% HClO4	One	AC 2.5 V	15±11 nm
J. Vac. Sci. Technol. B. **2008**, *26*, 1761	?	2E	Pt wire	≥37% HCl solution		0, 0.5, 1.0 V	≤50 nm
Rev. Sci. Instrum. **2013**, *84*, 073702	0.25 mm	2E	Pt ring	1 HCl:1ethanol	Two	DC, <2.5 V	<50 nm
Rev. Sci. Instrum. **2007**, *78*, 103702	0.125 mm			Aqua regia	Two		<50 nm
Rev. Sci. Instrum. **2012**, *83*, 015102	0.25 mm	2E	Pt foil	1 HCl:1EtOH	Two	40 V→20 V	±10 nm
Curr. Appl. Phys. **2011**, *11*, 1332	0.25 mm	2E	Pt loop	15wt% glycerol	Two	AC, 3 V	10 nm

Rev. Sci. Instrum. **2012**, *83*, 103708	0.2 mm	2E	W rod	1 HCl:1ethanol	One	DC, -15~+15 V	20 nm
J. Vac. Sci. Technol. B. **1995**, *13*, 1325	0.1 mm	2E	Au ring	≥37% fuming HCl	Four	DC, 0.5 V	<50 nm
Eur. Phys. J. Appl. Phys. **2005**, *31*, 139	0.25 mm	2E	Pt wire	HCl solution	Two	AC, 12 V	8~20 nm
Rev. Sci. Instrum. **2009**, *80*, 033701	0.25 mm	2E	Pt wire	38%HCl+96%H2SO4 (1:1)	One	AC, 2.5 V	20 nm
Rev. Sci. Instrum. **2011**, *82*, 026101	0.1 mm	2E	Carbon rod	37% fuming HCl+ demineralized water (1:1)	One	DC, 2.4 V	≈ 50 nm
Nanotech. **2011**, *22*, 025202	0.1 mm	2E	Pt ring	KCl solution	One	DC, 10 V	20~40 nm
J. Vac. Sci. Technol. B. **2010**, *28*, 631	0.1 mm	2E	Au ring	37%HCl+ethanol (1:1)	Three	DC, 1.8~2.2 V	?

2.3 Scanning Tunneling Microscopy (STM)

Scanning tunneling microscope (STM) is an instrument for imaging surfaces at the atomic level. Its development in 1981 earned its inventors, Gerd Binnig and Heinrich Rohrer (at IBM Zürich), the Nobel Prize in Physics in 1986.[28] For the STM, good resolution is considered to be 0.1 nm lateral resolution and 0.01 nm (10 pm) depth resolution.[29] With this resolution, individual atoms within materials are routinely imaged and manipulated. The STM can be used not only in ultra-high vacuum but also in air, water, and various other liquid or gas atmosphere, and at temperatures ranging from near zero kelvin to over 1000 ˚C.[30]

2.3.1 Theory and working principle of STM[31]

STM is the first member in the family of probe microscopes. Its working principle is based on the electron tunneling effect, in which an electron passes through the narrow potential barrier between a metal tip and a conducting sample in an external electric field (Figure 2.7).

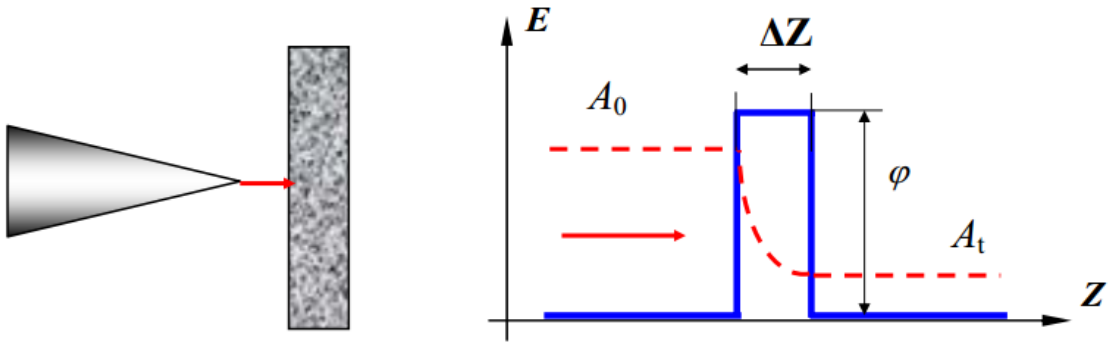

Figure 2.7. Scheme of electrons tunneling through a potential barrier in STM. Reproduced with permission from ref. 31.

The STM tip approaches the sample surface with a distance of several Angstroms. This forms a tunnel transparent barrier, the size of which mainly depends on the values of the work function for electron emission from the tip (φ_T) and from the sample (φ_S). The barrier can be evaluated by a rectangular shape with effective height equal to the average work function φ^*:

$$\varphi^* = \frac{1}{2}(\varphi_T + \varphi_S).$$

From the theory of quantum mechanics[32,33], the probability of electron tunneling (transmission coefficient) through one-dimensional rectangular barrier is:

$$W = \frac{|A_t|^2}{|A_0|^2} \cong e^{-k\Delta Z},$$

Where A_0 is the amplitude of electron wave function approaching the barrier; A_t the amplitude of the transmitted electron wave function, *k* the attenuation coefficient of the wave function inside the potential barrier; ΔZ the barrier width. In the case of tunneling between two metals, the attenuation coefficient is as below:

$$k = \frac{4\pi\sqrt{2m\varphi^*}}{h},$$

where *m* is the electron mass, φ^* the average work function of electron emission, *h* the Planck constant. Tunneling current will appear if a potential difference *V* is applied to the tunnel contact.

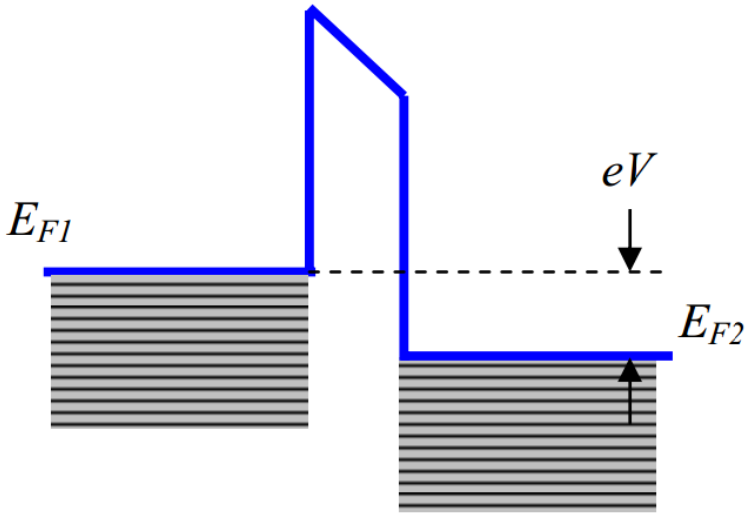

Figure 2.8. Energy level diagram of tunneling contact between two metals. Reproduced with permission from ref. 31.

Basically, electrons with energy near the Fermi level E_F participate in the tunneling process. In the case of contact between two metals, the current density can be expressed as following[34,35]:

$$j_t = j_0\left[\varphi^* \exp\left(-A\sqrt{\varphi^*}\Delta Z\right) - (\varphi^* + eV)\exp\left(-A\sqrt{\varphi^* + eV}\Delta Z\right)\right], \quad (1)$$

Where the parameters j_0 and A are set by the following expressions:

$$j_0 = \frac{e}{2\pi h(\Delta Z)^2}, \qquad A = \frac{4\pi}{h}\sqrt{2m}.$$

When the bias voltage is low ($eV < \varphi$), the current density can be approximated by a simpler expression. The first order approximation in the series expansion of $\left(-A\sqrt{\varphi^* + eV}\Delta Z\right)$ in expression (1) gives:

$$j_t = j_0 \exp\left(-A\sqrt{\varphi^*}\Delta Z\right) \cdot \left[\varphi^* - (\varphi^* + eV) \cdot \left(1 - \frac{AeV\Delta Z}{2\sqrt{\varphi^*}}\right)\right].$$

Finally, for $eV \ll \varphi^*$, we get:

$$j_t = j_0 \frac{A\sqrt{\varphi^*}eV\Delta Z}{2} \exp\left(-A\sqrt{\varphi^*}\Delta Z\right) = \frac{e^2\sqrt{2m\varphi^*}}{h^2} \cdot \frac{V}{\Delta Z} \exp\left(-\frac{4\pi}{h}\sqrt{2m\varphi^*}\Delta Z\right).$$

Because of the strong exponential dependence, a simpler formula is regularly used for estimations and qualitative reasoning:

$$j_t = j_0(V) e^{-\frac{4\pi}{h}\sqrt{2m\varphi^*}\Delta Z}, \qquad (2)$$

in which the value $j_0(V)$ is assumed to be not dependent on the tip-sample distance. For typical values (~4 eV) of the work function, the attenuation coefficient k is about 2 Å^{-1}. Therefore, the current value varies with one order of magnitude when ΔZ changes about 1 Å. Real tunneling contacts in the STM are not one-dimensional and have more complex geometry; however, the basic features of tunneling in more complex models are the same, as proved by experimental results.

For the high bias voltage ($eV > \varphi^*$), the well-known Fowler – Nordheim formula for electron field emission into vacuum is derived from expression (1):

$$J = \frac{e^3V^2}{8\pi h\varphi^*(\Delta Z)^2} \exp\left[-\frac{8\pi\sqrt{2m}(\varphi^*)^{\frac{3}{2}}\Delta Z}{3ehV}\right].$$

The exponential dependence (2) of the tunneling current on distance allows adjusting the tip-sample distance with high accuracy. The STM is an electromechanical system with a negative feedback. The feedback system *FS* keeps the tunneling current value at the constant level (I_0), selected by the operator. The control of the tunnel current value, and consequently of the tip-sample distance, is performed by moving the tip along the *Z* axis with the assistance of a piezoelectric element (Figure 2.9).

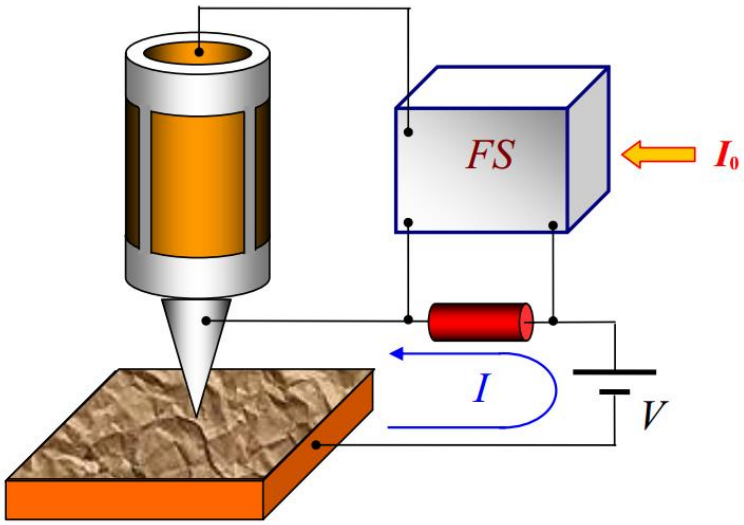

Figure 2.9. Simplified block-diagram of the feedback in STM. Reproduced with permission from ref. 31.

The image of a surface topography in STM is formed in two ways. In the constant current mode (Figure 2.10a), the tip moves along the surface to perform raster scanning; during this process, the voltage signal applied to the Z-electrode of a piezoelement in the feedback circuit is recorded into the computer memory as a *Z=f(x,y)* function, and is plotted by computer graphics then.

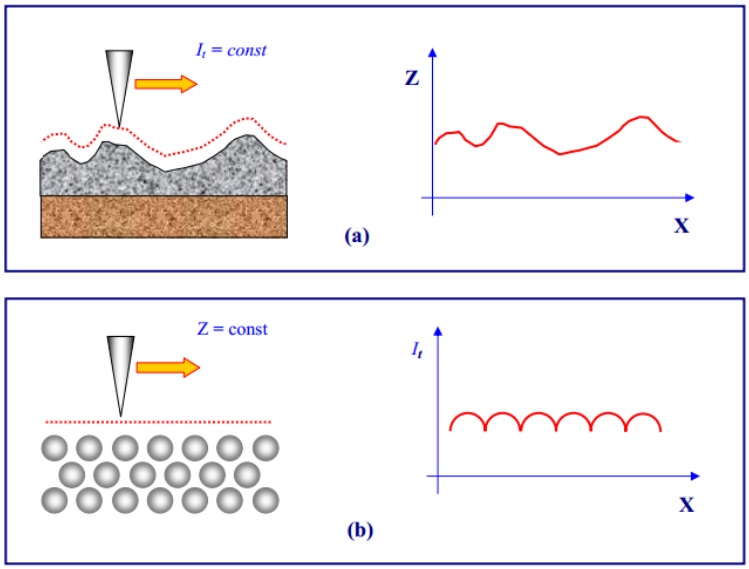

Figure 2.10. Formation of STM images in the constant current mode (a) and in the constant average distance mode (b). Reproduced with permission from ref. 31.

It is more effective to acquire the STM image in the constant height mode during investigation of atomic-smooth surfaces. In this case, the tip moves above the surface at a distance of several Angstrom; the tunneling current changes are recorded as STM image (Figure 2.10b). Scanning may be done either with the feedback system switched off (no topographic information is recorded), or at a speed exceeding the feedback response speed (only smooth changes of the surface topography are recorded). This way implements high scanning rate and fast STM images acquisition, allowing to observe the changes occurring on a surface in real time.

The high spatial resolution of the STM is due to the exponential dependence of the tunneling current on the tip-sample distance. The resolution in the direction normal to the surface can be achieved with fractions of Angstrom. The lateral resolution depends on the tip quality. Specifically, it is determined not by the macroscopic curvature radius of the tip apex, but by the atomic structure. If the tip was well prepared, there is either a single

projecting atom on its apex, or a small cluster of atoms, whose size is much smaller than the mean curvature radius. Actually the tunneling current flows between atoms on the sample surface and the tip atoms. The atom, protruding from the tip, approaches the surface to a distance comparable to the crystal lattice spacing. Since the dependence of the tunneling current on the distance is exponential, the current basically flows between the sample surface and the projecting atom on the tip apex.

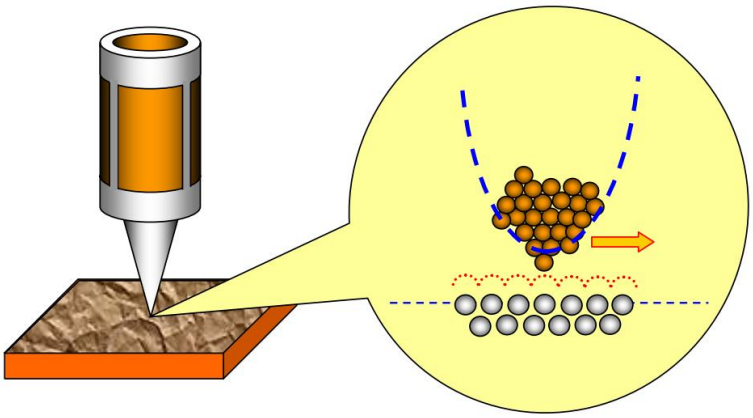

Figure 2.11. Atomic resolution in a scanning tunneling microscope. Reproduced with permission from ref. 31.

Using such tips, it is possible to achieve a spatial resolution down to atomic scale and thus many interesting researches.

2.3.2 Instrumentation of STM

The components of an STM include scanning tip, piezoelectric controlled height and x,y scanner, coarse sample-to-tip control, vibration isolation system, and computer.[36]

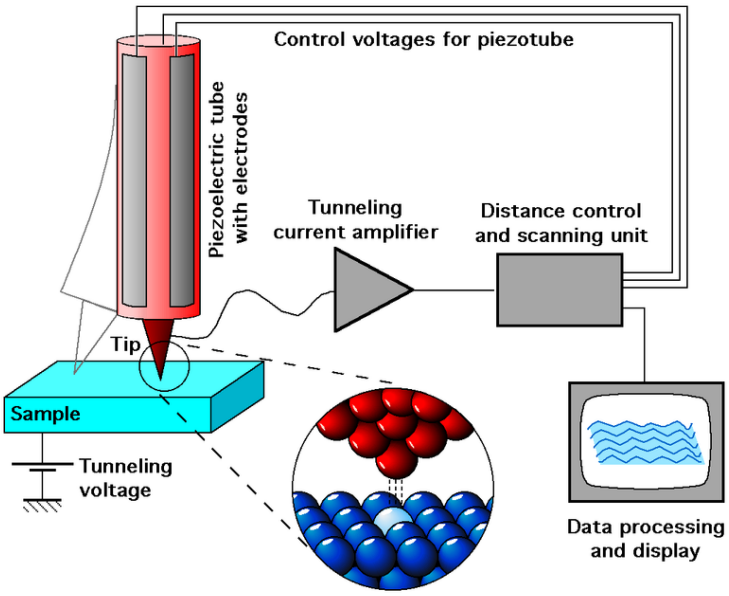

Figure 2.12. Schematic of the working principle of an STM (http://en.wikipedia.org).

The resolution of an image is limited by the radius of curvature of the scanning tip of the STM. Additionally, image artifacts can occur if the tip has two tips at the end rather than a single atom; this leads to “double-tip imaging”, a situation in which both tips contribute to the tunneling.[29] Therefore, it has been essential to develop processes for consistently obtaining sharp, usable tips. The tip is often made of tungsten or platinum-iridium. Tungsten tips are usually made by electrochemical etching, and platinum-iridium tips by mechanical shearing.[29]

Due to the extreme sensitivity of tunnel current to height, proper vibration insulation or an extremely rigid STM body is imperative for obtaining usable results. In the first STM by Binnig and Rohrer, magnetic levitation was used to keep the STM free from vibrations; now mechanical spring or gas spring systems are often used.[30] In addition, mechanisms for reducing eddy currents are sometimes implemented.

Maintaining the tip position with respect to the sample, scanning the sample and acquiring the data is computer controlled.[36] The computer may also be used for enhancing the image with the help of image processing[37,38] as well as performing quantitative measurements.[39,40]

2.4 References

1. Sergey, S. K.; Alexey, I. N.; Günter, G. H.; Joachim, L. *Nanotech.* **2011**, *22*, 025202.

2. Abadal, G.; Pérez-M., F.; Barniol, N.; Aymerich, X. *IEEE Trans. Instrum. Meas.* **2003**, *52*, 859.

3. Narasiwodeyar, S.; Dwyer, M.; Liu, M.; Park, W. K.; Greene, L. H. *Rev. Sci. Instrum.* **2015**, *86*, 033903.

4. Huang, T. X.; Huang, S. C.; Li, M. H.; Zeng, Z. C.; Wang, X.; Ren, B. *Anal. Bioanal. Chem.* **2015**, *407*, 8177.

5. Klein, M.; Schwitzgebel, G. *Rev. Sci. Instrum.* **1997**, *68*, 3099.

6. John, L. V.; Werner, K. *Thin Film Processes.* Academic, New York, **1978**.

7. Burke, M. G.; Sieloff, D. D.; Brenner, S. S. *J. Phys. (Paris).* **1986**, *47-C7*, 459.

8. Müller, E. W. *Z. Physik.* **1937**, *106*, 132.

9. Gomer, R. *J. Chem. Phys.* **1958**, *28*, 457.

10. Melmed, A. J.; Gomer, R. *J. Chem. Phys.* **1959**, *30*, 586.

11. Melmed, A. J. *J. Chem. Phys.* **1963**, *36*, 607.

12. Hibi, T. *J. Electronmicr.* **1956**, *4*, 10.

13. Hibi, T.; Ishikawa, K. *Sci. Rept. Res. Inst. Tohoku Univ.* **1961**, *13*, 311.

14. Binnig, G.; Rohrer, H.; Gerber, Ch.; Weibel, E. *Phys. Rev. Lett.* **1982**, *49*, 57.

15. Ren, B.; Picardi, G.; Pettinger, B. *Rev. Sci. Instrum.* **2004**, *75*, 837.

16. Billot, L.; Berguiga, L.; de la Chapellea, M. L.; Gilbert, Y.; Bachelot, R. *Eur. Phys. J. Appl. Phys.* **2005**, *31*, 139.

17. Wang, X.; Cui, Y.; Ren, B. *Chem. J. Chinese Univ.* **2007**, *28*, 522.

18. Eligal, L.; Culfaz, F.; McCaughan, V.; I. Cade, N.; Richards, D. *Rev. Sci. Instrum.* **2009**, *80*, 033701.

19. Lopes, M.; Toury, T.; de la Chapelle, M. L.; Bonaccorso, F.; Gucciardi, P. G. *Rev. Sci. Instrum.* **2013**, *84*, 073702.

20. Kharintsev, S. S.; Noskov, A. I.; Hoffmann, G. G.; Loos, J. *Nanotech.* **2011**, *22*, 025202.

21. Boyle, M.G.; Feng, L.; Dawson, P. *Ultramicroscopy* **2008**, *108*, 558.

22. Gingery, D.; Bühlmann, P. *Rev. Sci. Instrum.* **2007**, *78*, 113703.

23. Park, J.; Hong, T.; Lee, N.; Kim, K.; Seo, Y. *Curr. Appl. Phys.* **2011**, *11*, 1332.

24. Kharintsev, S.; Hoffmann, G.; Fishman, A.; Salakhov, M. K. *J. Phys. D Appl. Phys.* **2013**, *46*, 145501.

25. Libioulle, L.; Houbion, Y.; Gilles, J. M. *Vac. Sci. Technol. B* **1995**, *13*, 1325.

26. Quaade, U. J.; Oddershede, L. *Eur. Phys. Lett.* **2002**, *57*, 611.

27. Baykul, M. C. *Mater. Sci. Eng. B* **2000**, *74*, 229.

28. Ye, S.; Ishibashi, C.; Shimazu, K.; Uosaki, K. *J. Electrochem. Soc.* **1998**, *145*, 1614.

29. Binnig, G.; Rohrer, H. *IBM Journal of Research and Development* **1986**, *30*, 355.

30. Bai, C. New York: Springer Verlag, **2000**, ISBN 3-540-65715-0.

31. Chen, C. J. Oxford University Press, **1993**, ISBN 0-19-507150-6.

32. Mironov, V. L. *Fundamentals of Scanning Probe Microscopy*. Nizhniy Novgorod, **2004**.

33. Blohintsev, D. I. *Fundamentals of quantum mechanics.* Moscow, Nauka, **1983**.

34. Landau, l. D.; Lifshits, E. M. *Quantum Mechanics: non-relativistic theory.* Pergamon Press, Oxford, New York, **1977**.

35. Simons, J. G. *J. Appl. Phys.* **1963**, *34*, 1793.

36. Simons, J. G. *J. Appl. Phys.* **1963**, *34*, 2581.

37. Oura, K.; Lifshits, V. G.; Saranin, A. A.; Zotov, A. V.; Katayama, M. *Surface Science: an Introduction.* Berlin: Springer-Verlag **2003**, *ISBN 3-540-00545-5*.

38. *R. V. Lapshin. Rev. Sci. Instrum.**1995**, 66 4718.*

39. *R. V. Lapshin. Measur. Sci. Tech. **2007**, 18, 907.*

*40. R. V. Lapshin. Nanotech. **2004**, 15, 1135.*

41. R. V. Lapshin. Encyclopedia of Nanosci. Nanotech. **2011**, *14, 105.*

Chapter 3

Fabrication of Au tips by three-electrode electrochemical etching

3.1 Introduction

Au is one of the most commonly used materials to fabricate tips for a variety of local spectroscopies such as scanning tunneling microscopy (STM),[1-7] tip-enhanced Raman spectroscopy (TERS),[8-15] scanning near-field optical spectroscopy[16-19], electrochemical scanning tunneling microscopy (EC-STM)[20] and point-contact spectroscopy.[21] It has high free electron density and exhibits strong localized surface plasmon resonance (LSPR) in the visible and near-infrared regions.[18] In TERS, for example, the localized electric field generated near the tip surface due to LSPR can strongly enhance Raman signal. Second, Au has higher chemical stability than that of alkali metals and the other noble metals like silver in air or an aqueous environment, which allows Au tip can be used for several sets of experiments.[22]

Several methods to fabricate Au tips have been developed over the decades, mainly including the follows: (1) electrochemical etching,[19-23] (2) chemical polishing,[24] (3) ion milling,[25] (4) cathode sputtering,[26] (5) whisker growth[27-29] and (6) mechanical shaping.[30-32] Among them, electrochemical etching, in which a metal wire is anodically dissolved in an electrolyte, is widely used because of low cost and easy operation. In the previous work, a two-electrode electrochemical system consisting of a working electrode (WE) and a counter electrode (CE) has been applied to produce Au tips. However, etching conditions such as chemical species and concentration of the electrolyte, the applied potential and materials of the CE vary largely according to the electrochemical systems. In addition,

although the plasmon resonance wavelength and intensity strongly depend on tip shape,[33-36] the relationship between which and etching parameters has not been well clarified yet. In other words, the conventional methods with the two-electrode system have problems with controllability and reproducibility.

Here, we apply a three-electrode electrochemical system consisting of WE, CE and a reference electrode (RE) to fabricate Au tips for the first time. The Au tips are prepared by etching of the Au wires at a constant anodic potential which is precisely controlled against the potential of RE. The sharpness of the tips is well controlled and reproduced by controlling the applied potential.

3.1.1 Background

Au has several unique intrinsic properties as follows: (1) Strong LSPR effect in the visible region. Plasmon is an oscillation of electron density (cloud) in a metal, as illustrated in Figure 3.1. It has strong adsorption of light and can generate a localized electric field. (2) Higher chemical stability. Au has an electrochemical potential which is the lowest among metals.

Because of the several advantages, Au has been an excellent material for STM tips, as mentioned in *Chapter 1*. Au tips also have wide applications in other local spectroscopies (Figure 1.2). Therefore, it is of importance and necessity to fabricate smooth and sharp Au tips with high controllability and reproducibility.

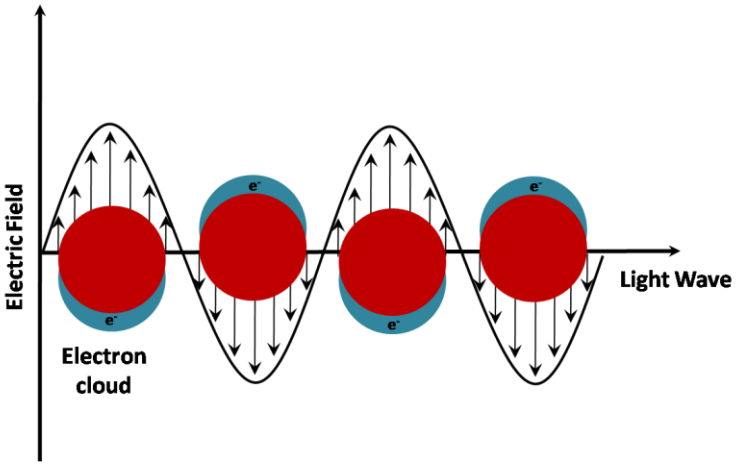

Figure 3.1. Schematic of electron cloud oscillation in nanoparticles. Transverse and longitudinal axes stand for the light wave and electric field, respectively. (http://www.nanovexbiotech.com/gold-nanoparticle-sensing/)

3.1.2 Fabrication methods

The conventional two-electrode electrochemical etching system (Figure 3.2a) has such advantages like low cost, easy operation and good reproducibility. It has simple etching principle, for example, in a Cl^- contained electrolyte, the reactions can be expressed as follows:

$$Au + 4Cl^- = AuCl_4^- + 3e^-, \qquad E_0 = 0.804\,V\ (vs.\,Ag/AgCl)$$

$$Au + 2Cl^- = AuCl_2^- + e^-, \qquad E_0 = 0.956\,V\ (vs.\,Ag/AgCl)$$

$$AuCl_2^- + 2Cl^- = AuCl_4^- + 2e^-, \qquad E_0 = 0.728\,V\ (vs.\,Ag/AgCl)$$

In comparison, a RE is introduced in the three-electrode system, which is shown in Figure 3.2b. A salt bridge connects an electrochemical cell and RE. It is a novel approach that has never been tried to fabricate Au tips.

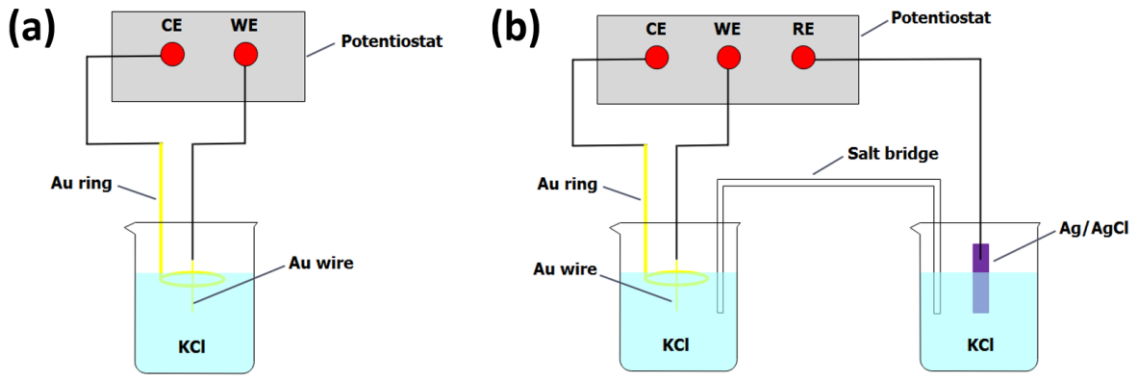

Figure 3.2. Schematics of the (a) two- and (b) three-electrode electrochemical etching system.

We used an Ag/AgCl reference electrode (Figure 3.3). It has some advantages: (1) fast electrode kinetics (100% efficiency), (2) a stable and well-known electrode potential (0.198 V), and (3) acts as reference in measuring and controlling the WE's potential and no point passes current. The dynamic equilibrium expressions are:

$Ag^+ + e^- \rightleftharpoons Ag\ (s)$

$AgCl\ (s) \rightleftharpoons Ag^+ + Cl^-$

Overall: $AgCl\ (s) + e^- \rightleftharpoons Ag\ (s) + Cl^-$

Figure 3.3. A picture of the Ag/AgCl reference electrode. (https://www.als-japan.com/1388.html)

3.1.3 Problems of conventional electrochemical method

First, etching conditions (electrolytes, applied potentials and CE materials) vary largely. Second, relationship between etching parameters and tip shape has not been well clarified, as already described in detail in Section 2.2; electric field enhancement and spatial resolution are closely related to tip shape (Figure 3.4).[37,38] Third, poor controllability and reproducibility.

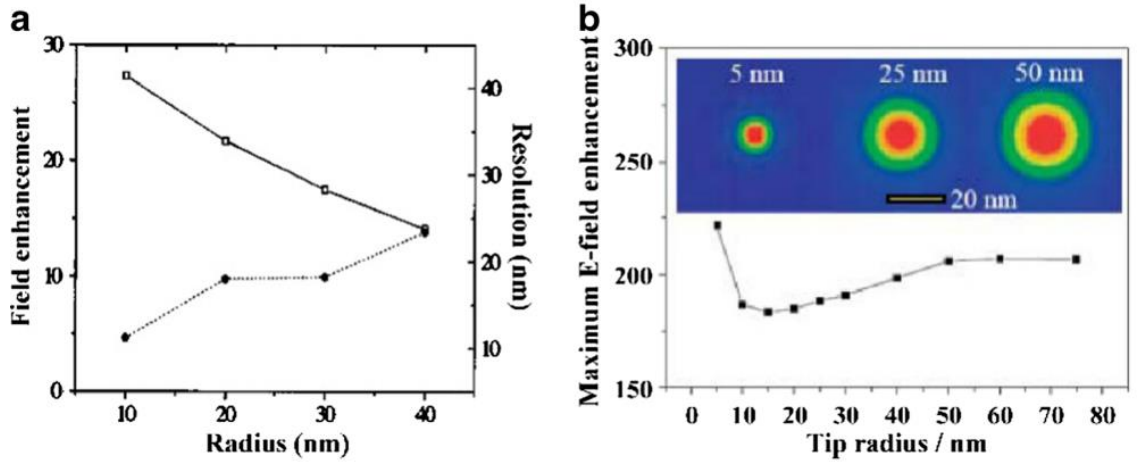

Figure 5. Effect of the tip radius on the field enhancement and spatial resolution between tip and substrate. (a) Silver tips couple with a glass substrate. Reproduced with permission from ref. 37. (b) Gold tips couple with gold substrate. Reproduced with permission from ref. 38.

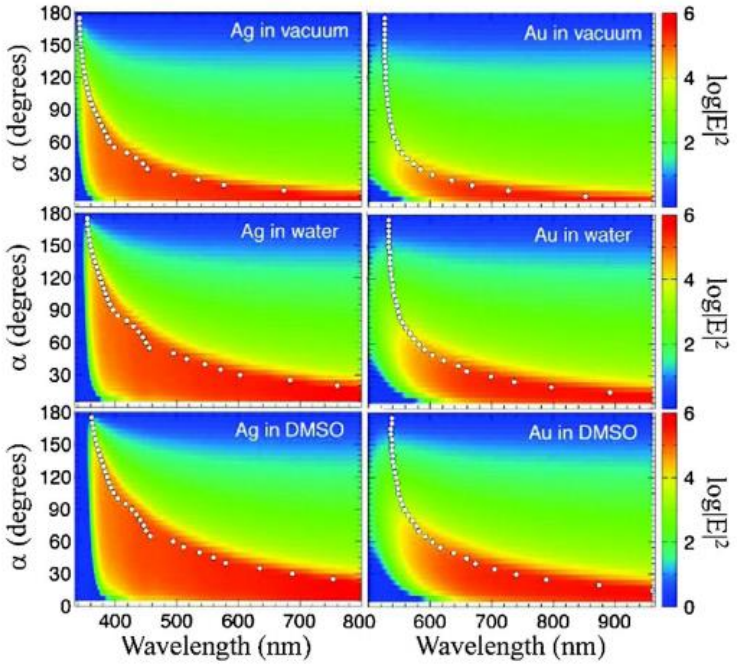

Figure 6. E-field intensities as a function of cone angel α and wavelength at 1 nm from the tip of the wedge. Reproduced with permission from ref. 39.

3.1.4 Goals

(1) To fabricate sharp Au tips with high controllability and reproducibility;

(2) Applications of Au tips in STM study.

3.2 Materials and set-up

3.2.1 Materials

An Au wire of 0.25 mm in diameter (99.95%, Nilaco Co.) annealed at 700 ˚C for 2 hours was used as a WE to prepare the tips. An Au ring with a diameter of 1 cm made of the 0.50 mm diameter wire was employed as a CE. An Ag/AgCl/saturated KCl electrode (ALS Co., Ltd) was applied as a RE. The electrolyte was a 2.79 mol·L^{-1} KCl (Wako Pure Chemical Industries, Ltd.) aqueous solution. A salt bridge was made from the saturated KCl aqueous solution and agar (Wako Pure Chemical Industries, Ltd.).

3.2.2 Experimental set-up

The Au ring was immersed into the solution and then lifted up to form a meniscus at the interface between the ring and solution. The Au wire was positioned at the center of the ring and immersed in the solution with ~1 mm in depth. The Au tips were fabricated by the three-electrode electrochemical etching system (Figure 3.2b). The applied DC potential to the WE was 1.1-1.5 V, which was precisely controlled against RE. By using a potentiostat (VersaSTAT 4, Princeton Applied Research), the real-time change of anodic current during etching was monitored. The etching process was automatically terminated at an optimal set point in order to avoid the problem of over-etching.[8] The as-prepared

tips were carefully washed with ultrapure water to remove residual impurities on the surface.

3.3 Experimental

3.3.1 Cyclic voltammetry (CV) measurement

Electrochemical reactions on the Au wire were analyzed with the CV measurements which provide quantitative information on oxidation and reduction reactions. The CV measurements were performed in the potential region between -0.4 V and 1.1-1.5 V with the same electrochemical set-up as used for Au tip fabrication. Both the initial and end points for the scan were fixed at -0.4 V and the turning point was set at 1.1, 1.2, 1.3, 1.4 and 1.5 V. The scan rate was 0.01-1.0 V/s.

Figure 3.5 shows CV curves on the Au wire obtained in the KCl aqueous solution in the potential range between -0.4 V and 1.1, 1.2, 1.3, 1.4 and 1.5 V, with sweep rate of 1 V/s.

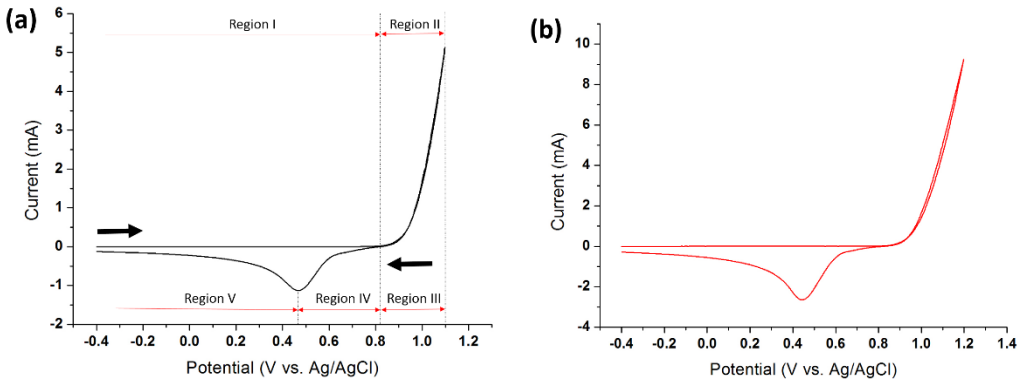

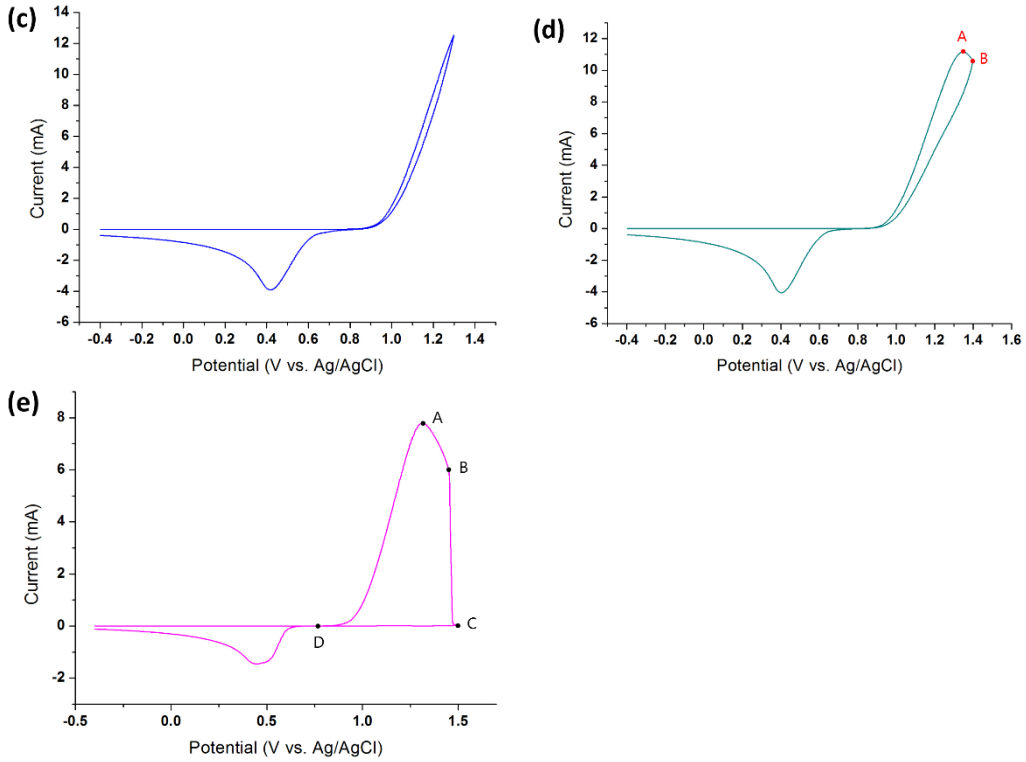

Figure 3.5. CV curves on the Au wire obtained in the KCl aqueous solution in the potential range between -0.4 V and 1.1, 1.2, 1.3, 1.4 and 1.5 V, with a sweep rate of 1 V/s.

The onset potential of oxidation is 0.83 V in the positive potential sweep, and the anodic current increases almost linearly until 1.3 V. The oxidation process of the Au electrode was investigated in a sulfuric acid solution containing chloride ions (Cl^-) and two possible oxidation reactions were proposed.[40]

$$Au + 4Cl^- = AuCl_4^- + 3e^-, \qquad E_0 = 0.804\,V\ (vs.\,Ag/AgCl) \tag{1}$$

$$Au + 2Cl^- = AuCl_2^- + e^-, \qquad E_0 = 0.956\,V\ (vs.\,Ag/AgCl) \tag{2}$$

The in situ measurement of the dissolution of Au with an electrochemical quartz crystal microbalance clearly demonstrated that Au dissolves through the $3e^-$ oxidation reaction.[40]

In the presence of Cl^-, the adsorption of Cl^- on the Au surface suppresses the formation of Au oxides.[40] Our observed onset potential (0.83 V) almost corresponds to the reported value of the reaction (1). Therefore the Au wire is dissolved in the KCl solution in the anodic potential range between ~0.83 V and ~1.3 V (Figure 3.5a-c). The anodic peak was observed at ~1.34 V (Figure 3.5d, point A), and the current continuously decreases at the higher potentials. The previous study revealed that there is a potential boundary between the lower potential region where the dissolution reaction is dominant and the higher potential region where both the dissolution and the oxide formation reactions occur at the same time.[40] Thus, the decrease in the anodic current at > 1.34 V results from the competitive reactions between the dissolution of Au and the formation of Au oxides which act as a passivation layer to inhibit the dissolution process. In addition, a sudden drop at ~1.45 V was observed (Figure 3.5e, point B). This is attributed to the surface of the Au wire fully covered with the oxide film.

In the negative potential sweep shown in Figure 3.5a-d, a cathodic peak appears at 0.4-0.45 V due to the reduction reaction of $AuCl_4^-$ formed by the dissolution of Au. Intensities and positions of the peaks depend on the amount of $AuCl_4^-$ species. In contrast, once the Au surface is fully covered with the Au oxide film (Figure 3.5e), no current flows until ~0.6 V and a broad cathodic peak was observed. In the case of the CV curve of the Au electrode obtained in $HClO_4$ solution containing Cl^-, two cathodic peaks of the reduction of Au oxides and $AuCl_4^-$ were detected and the peak at the more positive potential was identified as the dissolution of the oxides.[40] Therefore, the broad peak consists of two overlapped peaks corresponding to the reduction reactions of the Au oxides and $AuCl_4^-$, and the reduction of the Au oxides occurs prior to the reduction of $AuCl_4^-$.

Next we overlapped the CV curves of the Au wire obtained in the KCl aqueous solution in the potential range between -0.4 V and 1.1, 1.2, 1.3, 1.4 and 1.5 V with sweep rate of 1 V/s, as shown in Figure 3.6.

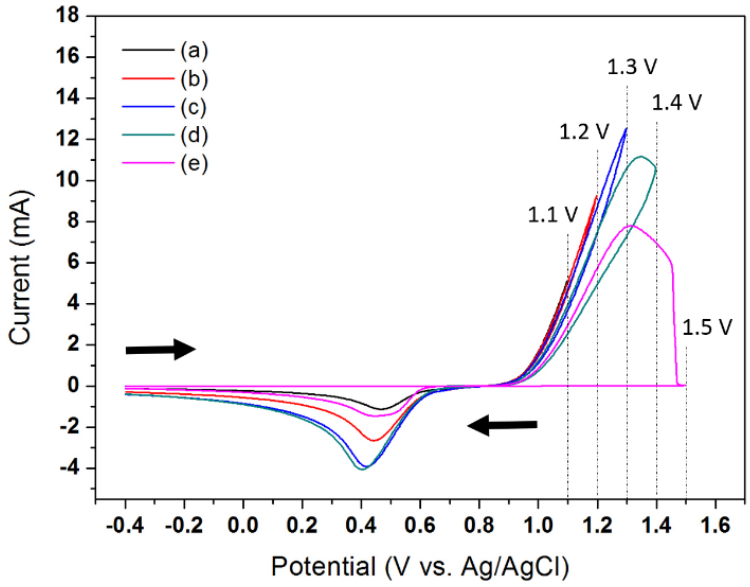

Figure 3.6. Overlapping of the CV curves of an Au wire of 0.25 mm in diameter obtained in the 2.79 mol·L^{-1} KCl aqueous solution in the potential region between -0.4 V and (a) 1.1, (b) 1.2, (c) 1.3, (d) 1.4 and (e) 1.5 V. The CV curves were successively obtained from (a) to (e) with the same Au wire. Sweep rate is 1 V/s.

In addition, the dependence relationship between sweep rate and CV was also investigated. Figures 3.7 and 3.8 indicate the corresponding results obtained at 0.01 V/s and 0.1 V/s, respectively. As a whole, the variation tendencies are similar with the case of 1 V/s, but still have some differences. Specifically, fluctuations appear during the scan in range from -0.4 V to 1.4/1.5 V, at 0.01 V/s. The position starts from 1.2 V and ends at 1.4 V (Figure 3.7d, e). The current is always larger than zero during negative scan, and both all

the curves perfectly coincide in the range of -0.4 V and 0.8 V. It is noteworthy that the negative-scan current has same tendency with positive-scan one when the potential is less than 1.4 V, in the range from -0.4 V to 1.5 V (Figure 3.7e). At 0.1 V/s, however, the result presents its own distinguishing features. Although the noises disappear, yet the shape at high potential differs. And reduction reaction starts to occur (0.4 V-0.6 V).

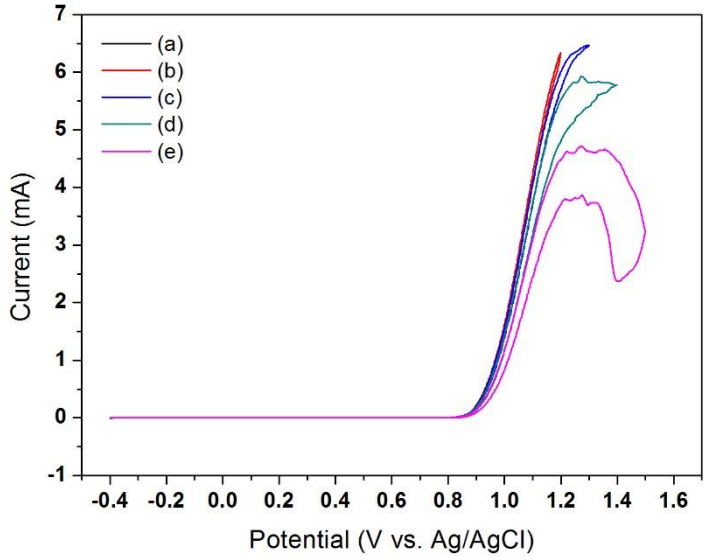

Figure 3.7. Overlapping of the CV curves of an Au wire of 0.25 mm in diameter obtained in the 2.79 mol·L^{-1} KCl aqueous solution in the potential region between -0.4 V and (a) 1.1, (b) 1.2, (c) 1.3, (d) 1.4 and (e) 1.5 V. The CV curves were successively obtained from (a) to (e) with the same Au wire. Sweep rate is 0.01 V/s.

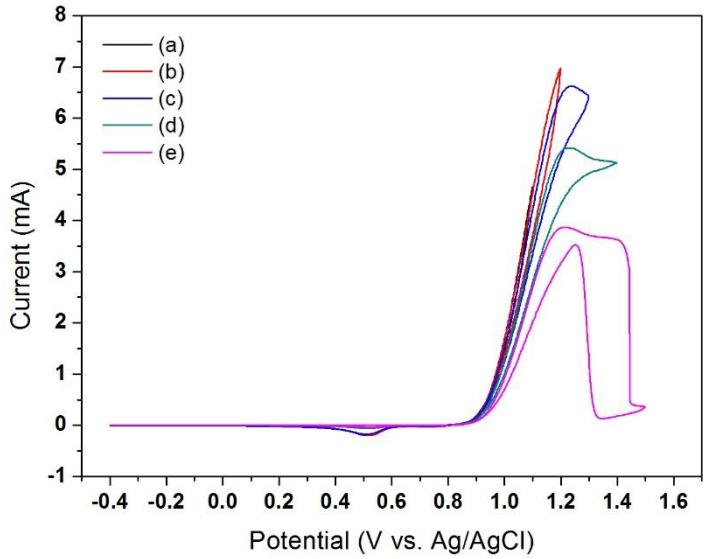

Figure 3.8. Overlapping of the CV curves of an Au wire of 0.25 mm in diameter obtained in the 2.79 mol·L^{-1} KCl aqueous solution in the potential region between -0.4 V and (a) 1.1, (b) 1.2, (c) 1.3, (d) 1.4 and (e) 1.5 V. The CV curves were successively obtained from (a) to (e) with the same Au wire. Sweep rate is 0.1 V/s.

3.3.2 Current-etching time (*I-t*) measurement

The Au tips were prepared by applying a constant potential to the Au wire according to the CV curves. The intensity of the anodic current is proportional to the surface area of the Au wire immersed in the solution, and thus the current trace reflects the progress of etching. Figure 3.9 show the applied potential dependence of I-t curves. The annealing temperature is 300 ˚C. The annealing time are (a) 2 h, (b) 5 h, (c) 8 h, and (d) 12 h, respectively. From the following results, we can see that the applied potential largely affects the etching time. So the etching time is the longest (~480 s) at 1.1 V. The etching

time remarkably decreases when the potential is 1.2 V. Notably, only the dissolution reaction is induced at ≤1.3 V, but on the other hand, both the dissolution and oxide formation reactions occur at 1.4 V as described above. In addition, several spike peaks appear in the current trace during etching at 1.4 V due to the formation of bubbles resulting from the generation of Cl_2 gas on the Au wire. The sudden drop of the current right after applying potential at 1.5 V is attributed to a rapid formation of the passivation layer of the Au oxide.

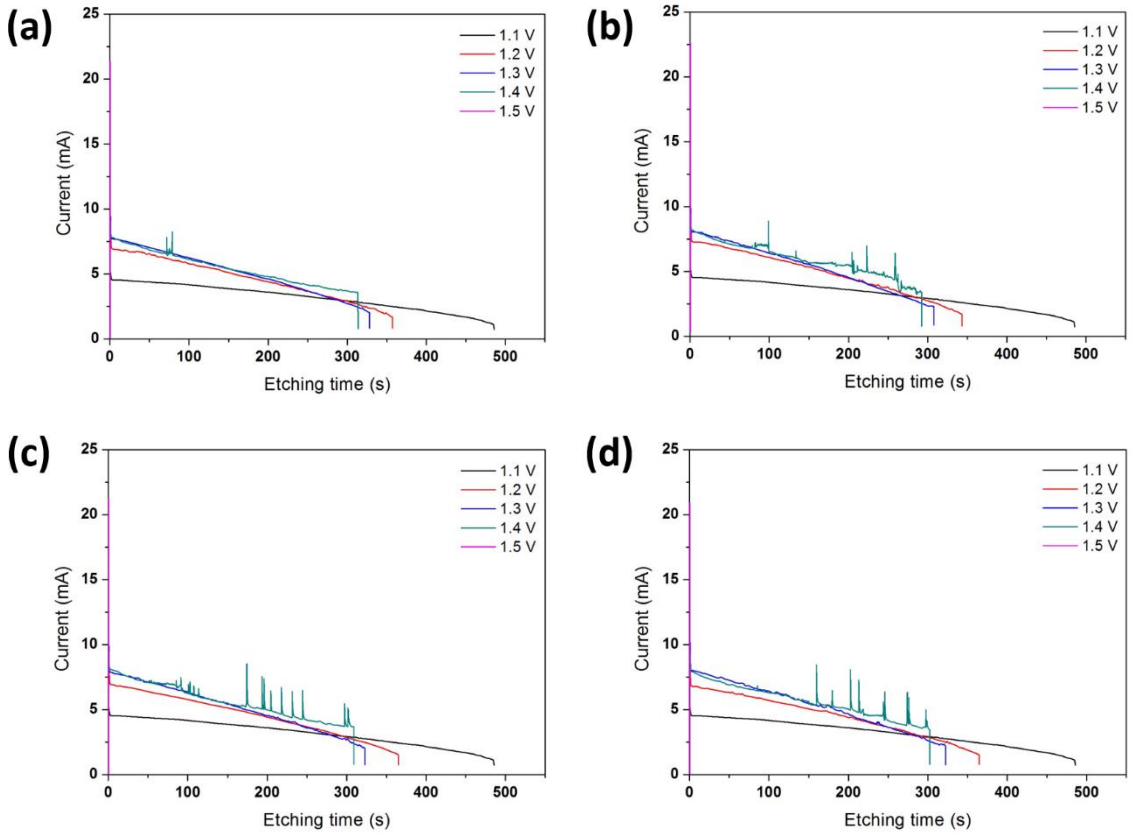

Figure 3.9. Applied potential dependence of I-t curves for the Au wires annealed at different time: (a) 2 h, (b) 5 h, (c) 8 h, and (d) 12 h, respectively. The annealing temperature is 300 ˚C.

The Au wires were also annealed at other temperatures, including 500 ˚C, 700 ˚C, and

900 ˚C. Figure 3.10, Figure 3.11, and Figure 3.12 are the according experimental results, respectively.

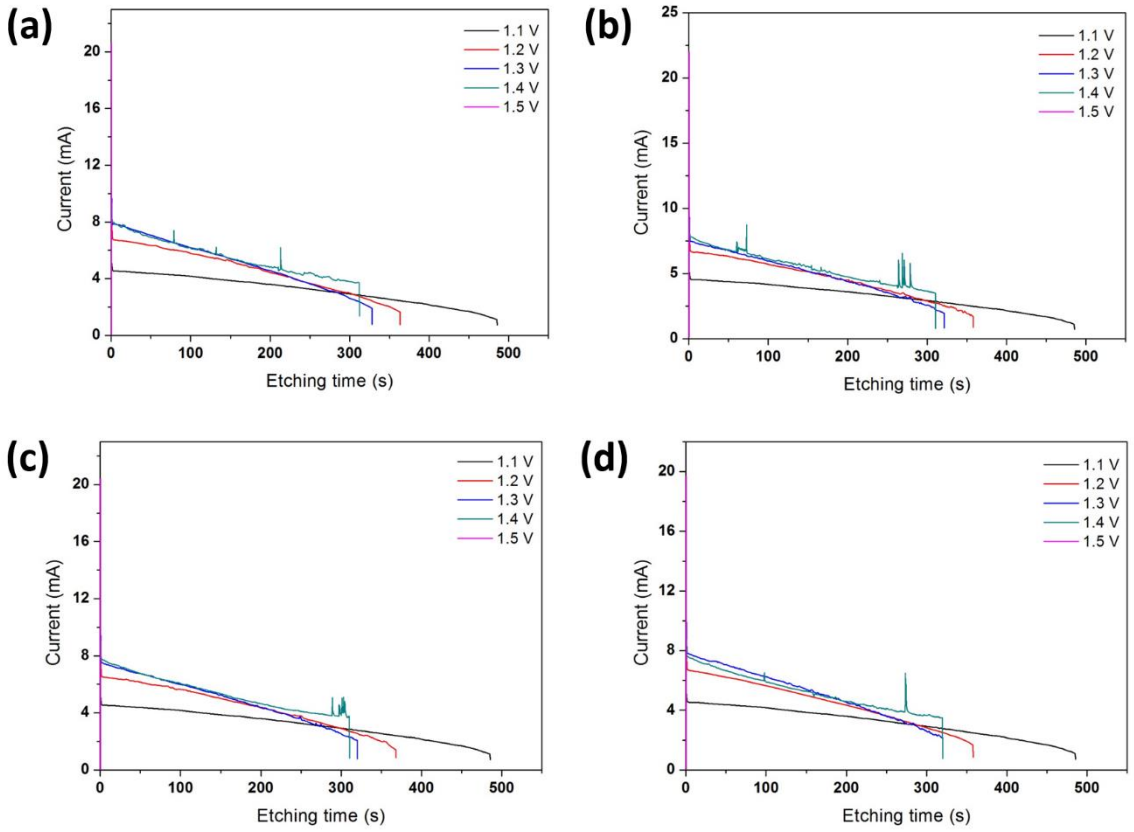

Figure 3.10. Applied potential dependence of I-t curves for the Au wires annealed at different time: (a) 2 h, (b) 5 h, (c) 8 h, and (d) 12 h, respectively. The annealing temperature is 500 ˚C.

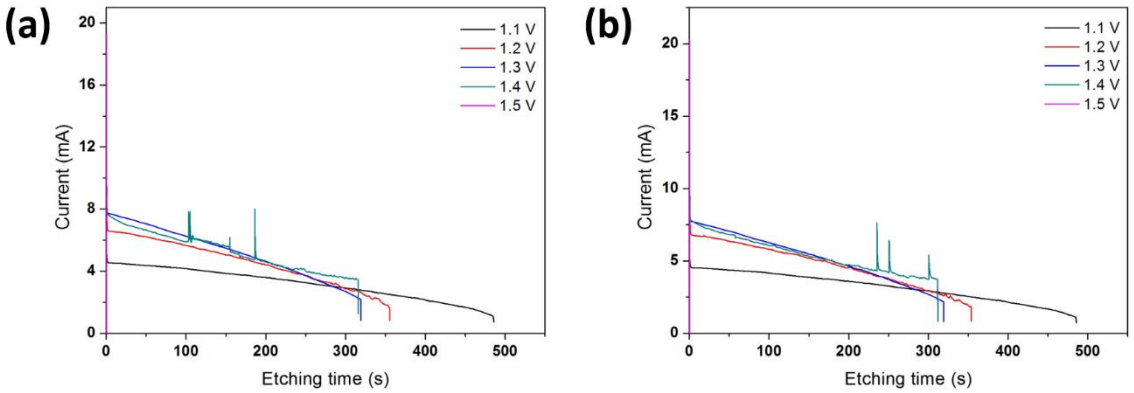

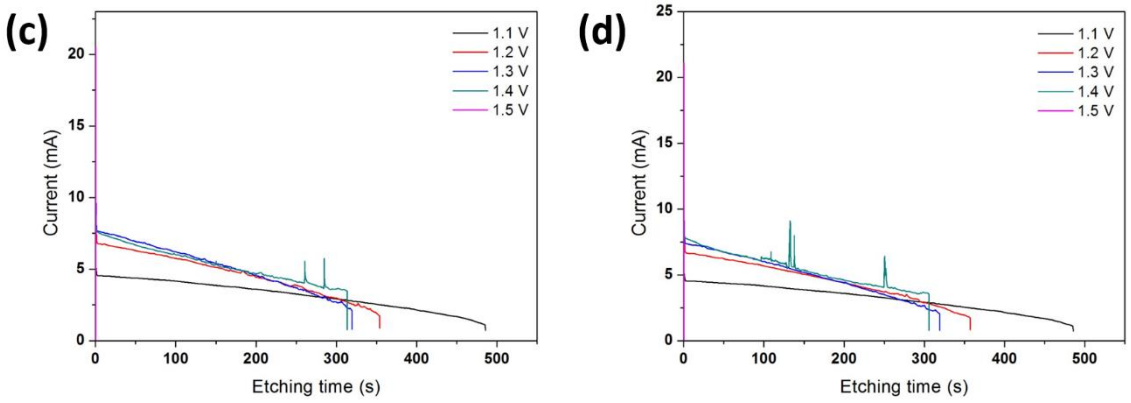

Figure 3.11. Applied potential dependence of I-t curves for the Au wires annealed at different time: (a) 2 h, (b) 5 h, (c) 8 h, and (d) 12 h, respectively. The annealing temperature is 700 ˚C.

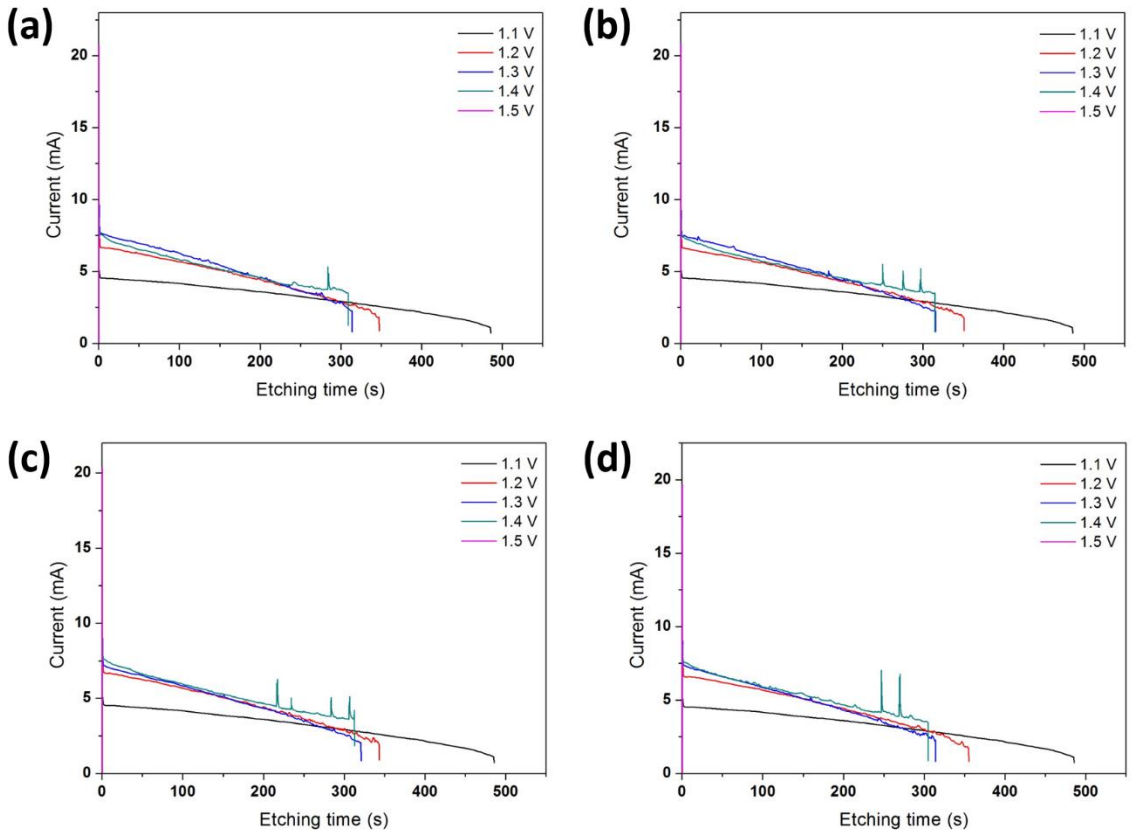

Figure 3.12. Applied potential dependence of I-t curves for the Au wires annealed at different time. The annealing temperature is 900 ˚C.

These results are so similar that we can't determine which annealing condition is the optimal. SEM characterization is good way to solve the problem, which will be discussed in the following.

3.3.3 A scanning electron microscope (SEM)

The Au tips were observed with a field emission scanning electron microscope (FE-SEM, JSM-6330F, JEOL) to evaluate a radius of curvature (R) and a cone angle (θ). The accelerating voltage and working distance were 20 kV and 8 mm, respectively.

First of all, to illustrate the importance of annealing treatment, we selects four typical tips: tip 1 and tip 2 are prepared with an as-received Au wires; tip 3 and tip 4 are fabricated with the wires annealed at 300 ˚C for 2 hours. The applied potential are same (1.3 V). The FE-SEM images are indicated in Figure 3.13. Tips 1 and 2 (Figure 3.13a, b) have rough and sawteeth-like surfaces, thus it is difficult to estimate the radius of curvature. On the contrary, the tips fabricated with annealed wires have very smooth surface and sharp end, seen from Figure 3. 13c, d. This mainly resulted from the better crystallization after annealing treatment, during which the grains gradually grow up and combine with each other, approaching to form a single crystal.[19,21]

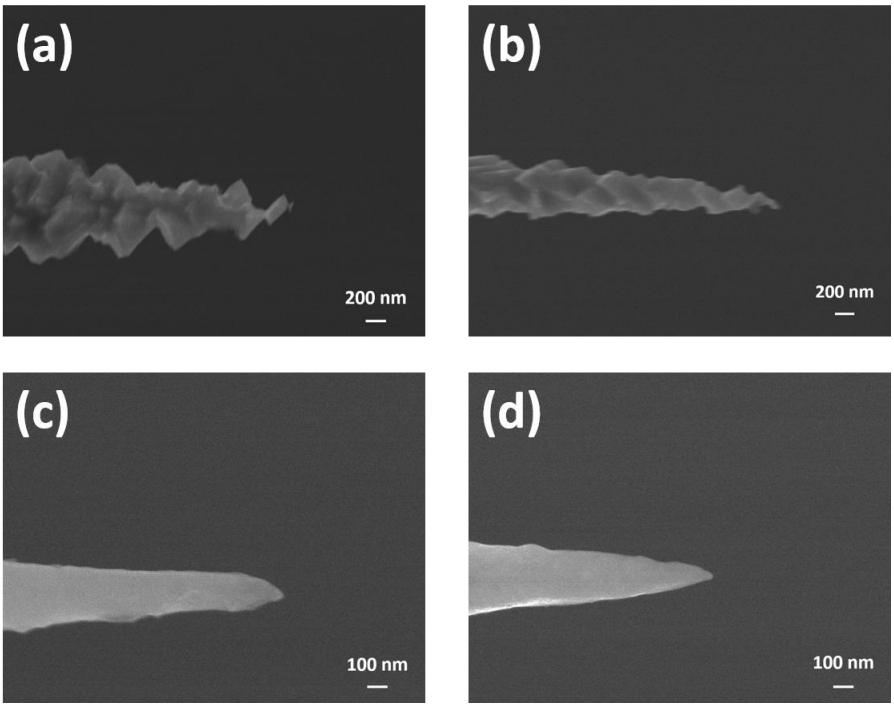

Figure 3.13. Field emission-scanning electron microscope images of the typical Au tips. (a), (b) stand for tip 1 and tip 2, which are fabricated with the as-received wires. (c), (d) stand for tip 3 and tip 4, which are fabricated with the annealed wires. The annealing condition is 300 ˚C for 2 h.

A variety of annealing treatments were adopted to the as-received Au wires. The annealing temperatures are 300 ˚C, 500 ˚C, 700 ˚C and 900 ˚C, respectively. The annealing time includes 2, 5, 8, and 12 h. Figure 3.14-17 are the applied potential dependences of the SEM images of tips prepared by using the Au wires annealed at 300 ˚C but with different hours. These results are very similar and the tip radius can be decades of nanometers even the pre-annealing time is 2 hours. So for energy and time saving, we selected “2 hours” as the optimal annealing time.

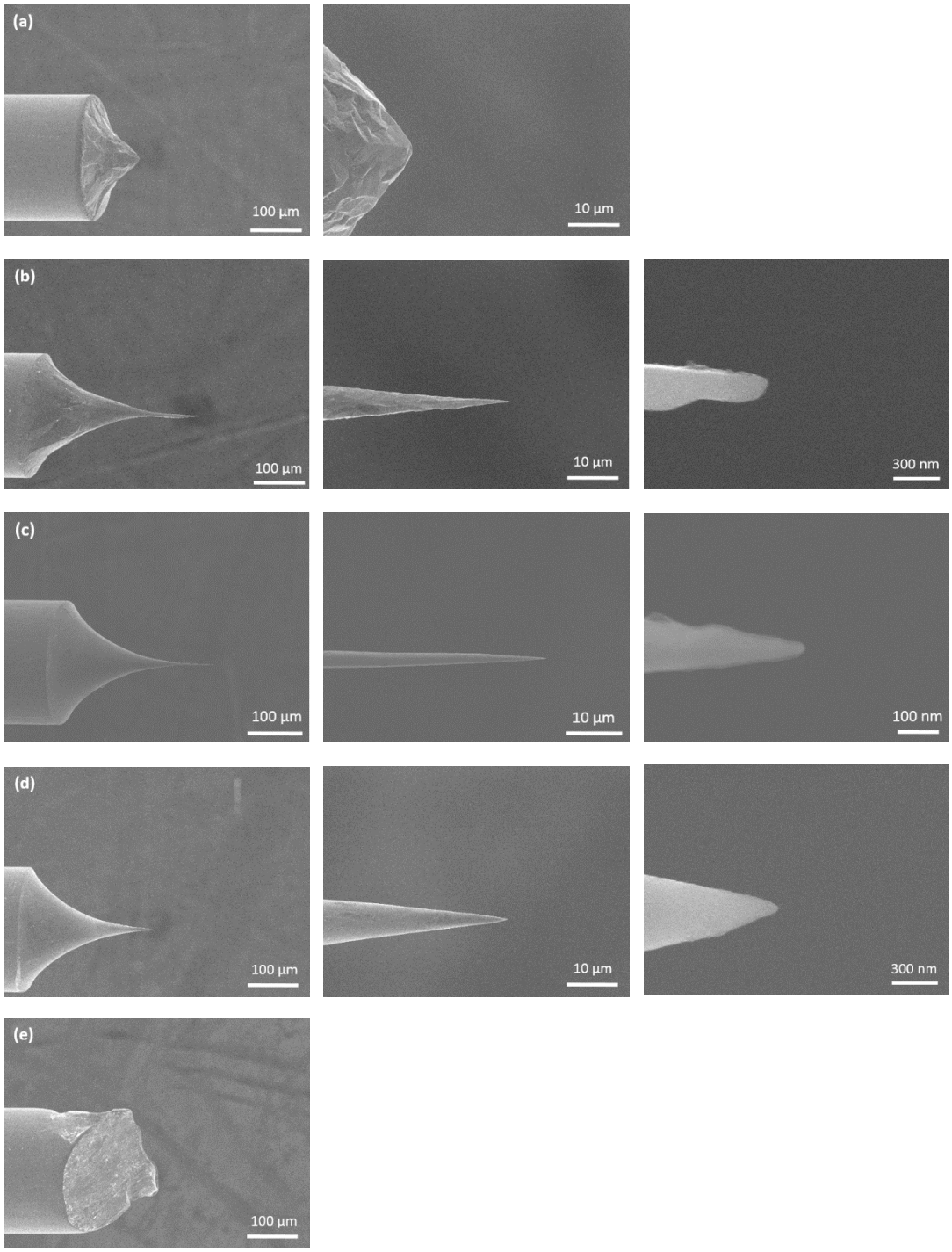

Figure 3.14. FE-SEM images of the Au tips fabricated at different applied potentials by using the wires annealed at 300 ˚C for 2 h. (a) 1.1 V, (b) 1.2 V, (c) 1.3 V, (d) 1.4 V, and (e) 1.5 V.

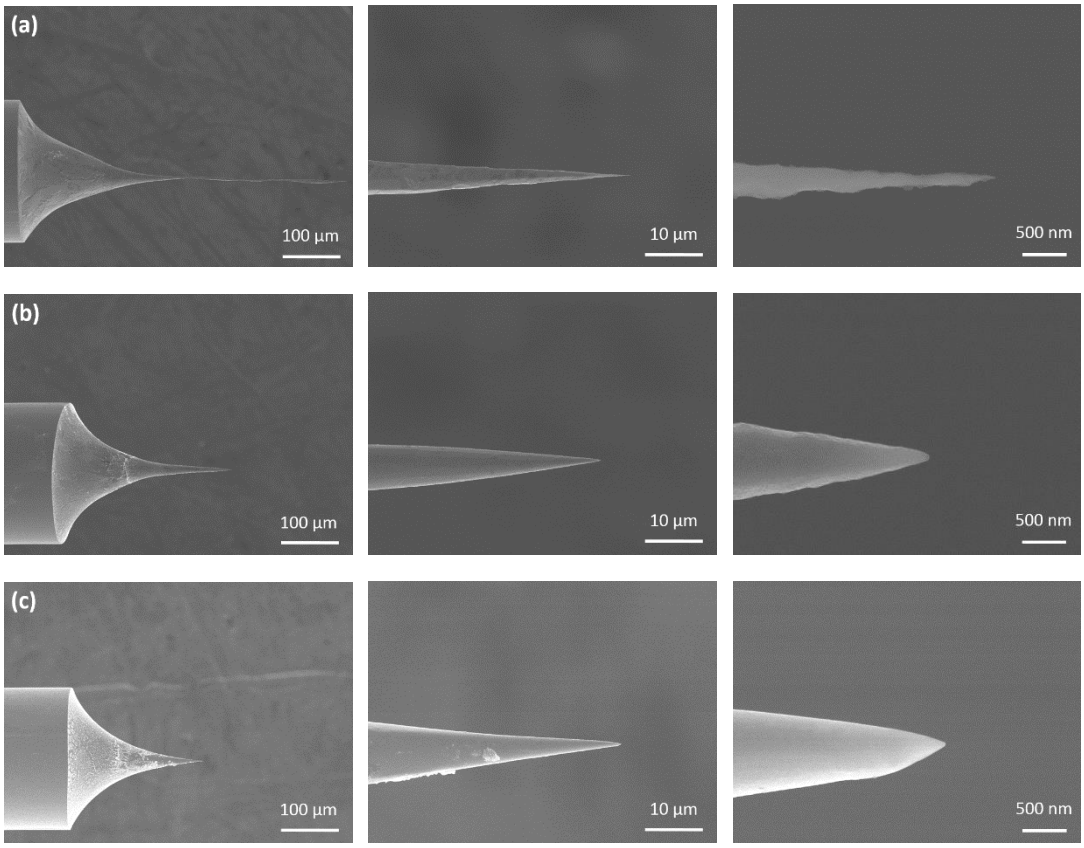

Figure 3.15. FE-SEM images of the Au tips fabricated at different applied potentials by using the wires annealed at 300 ˚C for 5 h. (a) 1.2 V, (b) 1.3 V, and (c) 1.4 V.

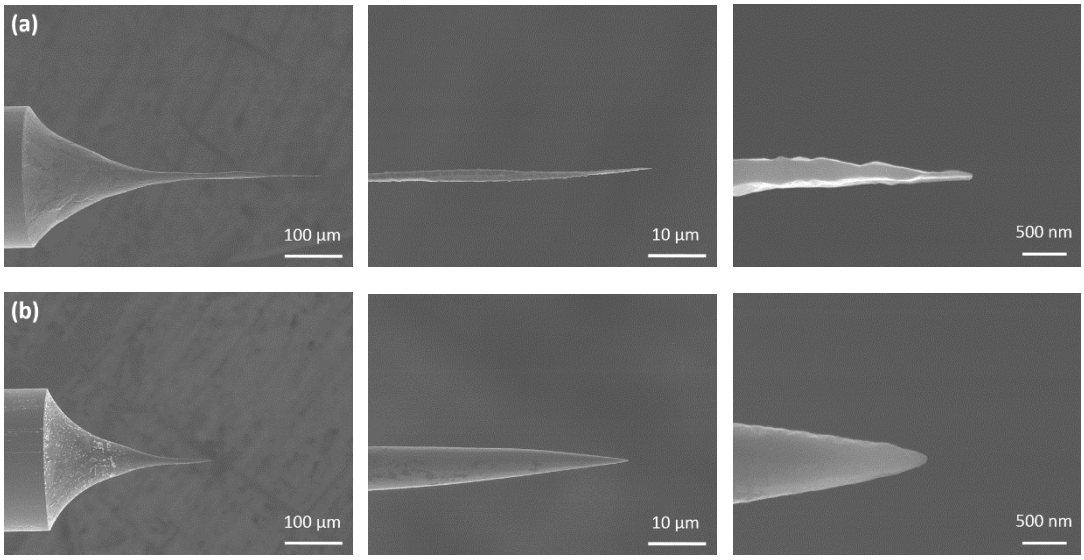

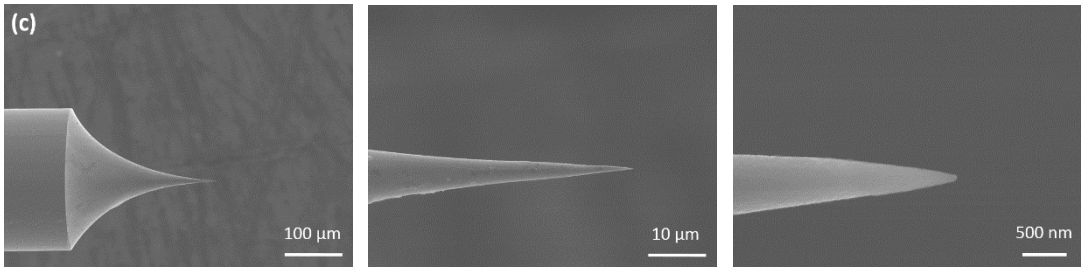

Figure 3.16. FE-SEM images of the Au tips fabricated at different applied potentials by using the wires annealed at 300 ˚C for 8 h. (a) 1.2 V, (b) 1.3 V, and (c) 1.4 V.

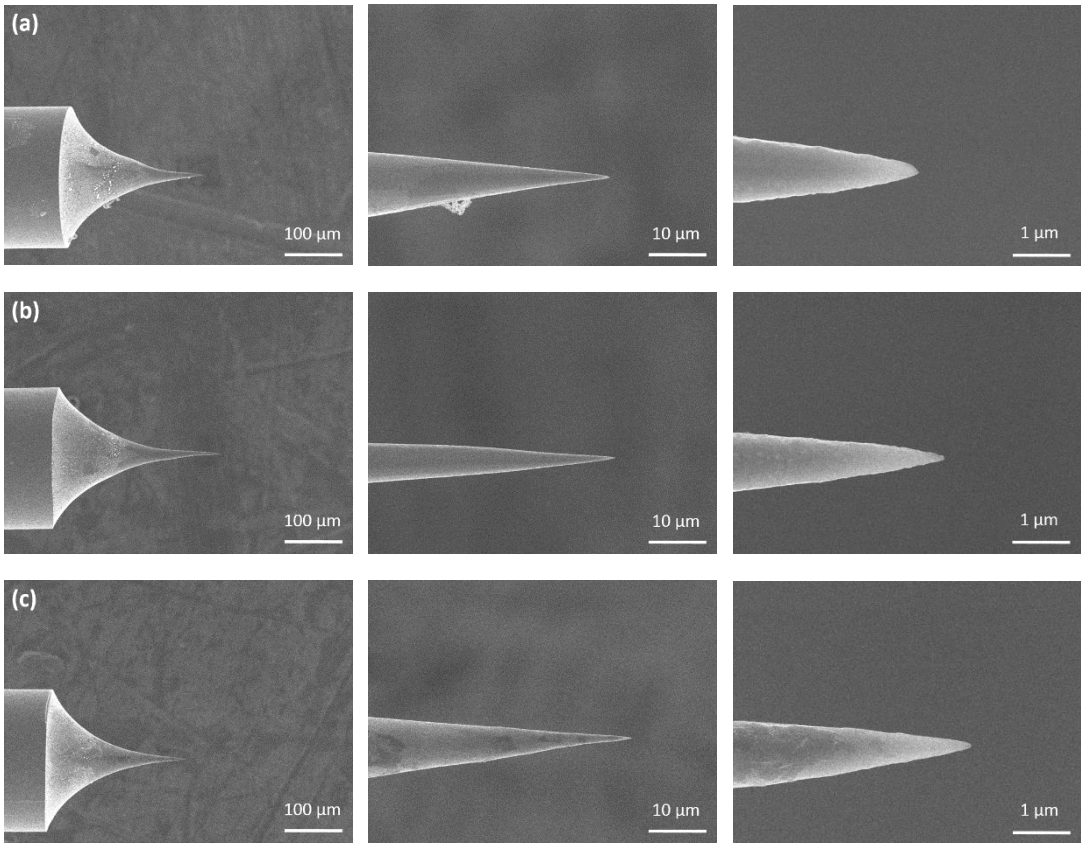

Figure 3.17. FE-SEM images of the Au tips fabricated at different applied potentials by using the wires annealed at 300 ˚C for 12 h. (a) 1.2 V, (b) 1.3 V, and (c) 1.4 V.

After many trials, we found that the average radius of tips can be the smallest when the 700 ˚C annealed wires were used. Figure 3.18 shows the typical SEM images of Au tips

fabricated at 1.3 V by using the wires annealed at 700 ˚C for 2 h. Therefore, the optimal annealing condition is “700 ˚C, 2 h”.

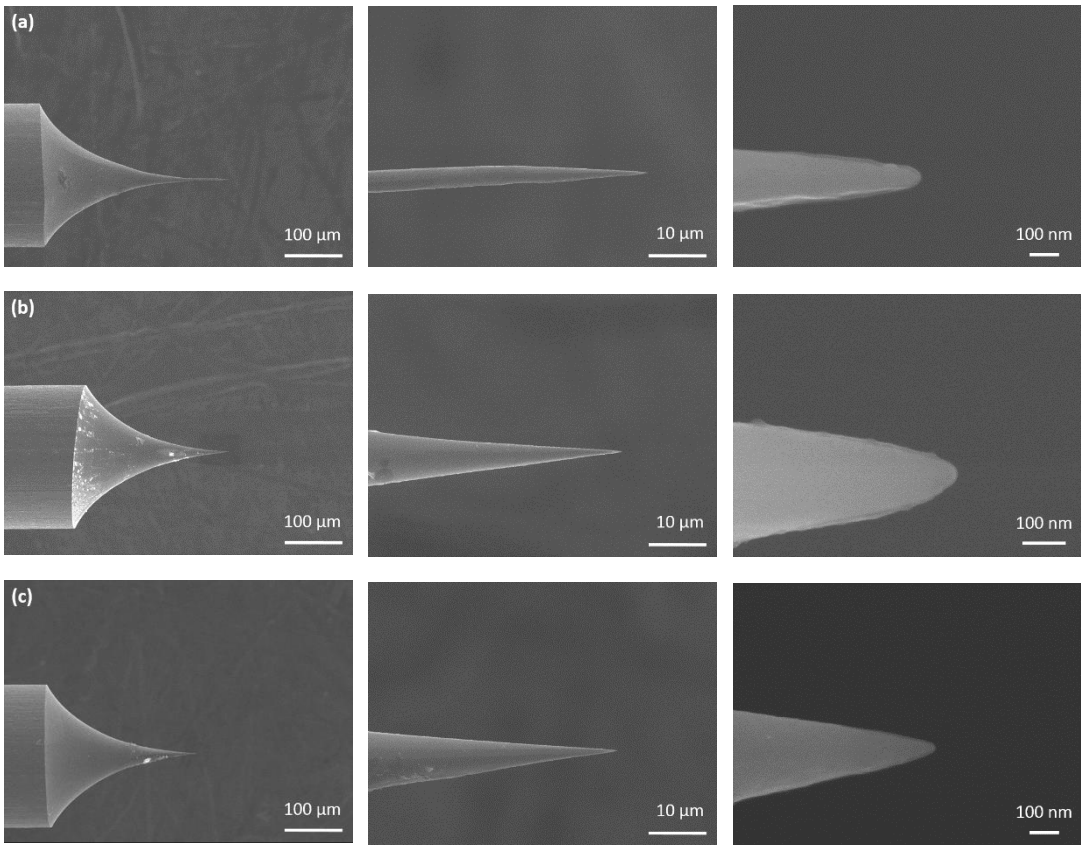

Figure 3.18. FE-SEM images of three Au tips fabricated at 1.3 V by using the wires annealed at 700 ˚C for 2 h.

The dependence relationship between applied potential and tip morphology was investigated, as shown in Figure 3.19. We can see that the whole shape of Au tips is closely related to the applied potential. Besides, the length of etched part shortens as the applied potential increases from 1.1 to 1.4 V. According to the videos recording the etching processes, the final shape of the tips is not determined by the shape of the meniscus but by the reaction rate controlled by the applied potential, because the tip was still immersed in the solution after the etching was stopped. The shape of the wire didn’t change at 1.5 V,

which corresponds to the current change shown in Figure 3.9.

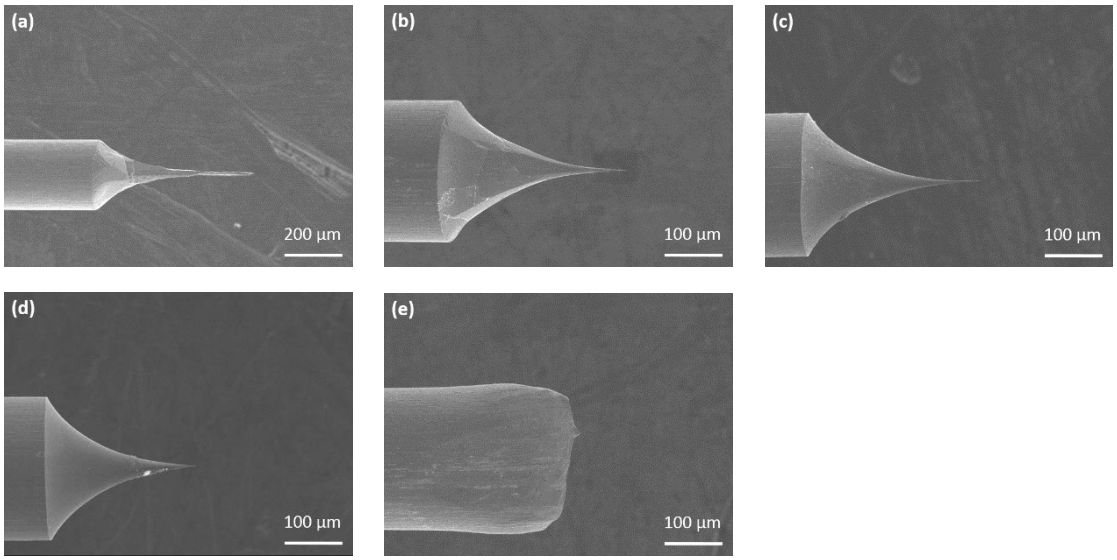

Figure 3.19. Low magnified FE-SEM images of the Au tips fabricated under different applied potentials. (a) 1.1 V, (b) 1.2 V, (c) 1.3 V, (d) 1.4 V and (e) 1.5 V.

With the SEM data, length of etched part (*L*) of the Au tips prepared at different applied potentials was measured. Figure 3.20a is schematic of the tip shape. Figure 3.20b are the values of *L* of six tips at 1.1 V, 1.2 V, 1.3 V, and 1.4 V. The value is larger than 500 µm at 1.1 V. However the *L* shortens to ~300 µm when the potential increases to 1.2 V and 1.3 V, and becomes much shorter at 1.4 V.

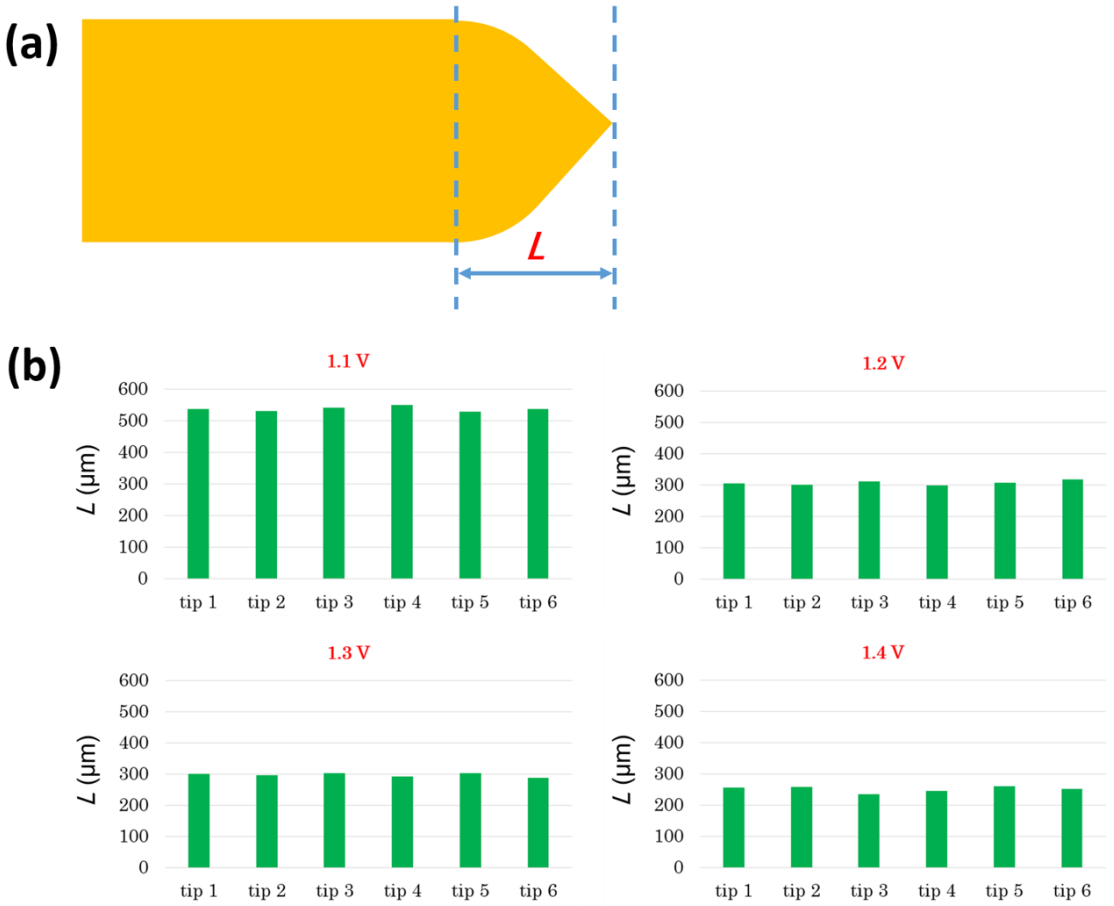

Figure 3.20. Length of etched part (L) of the Au tips prepared at different applied potentials. (a) Schematic of the tip shape, indicating L. (b) The values of L of six tips at 1.1 V, 1.2 V, 1.3 V, and 1.4 V.

3.3.4 Radius (R) and cone angle (θ)

The LSPR properties of plasmonic tips are evaluated by a radius of curvature (R) and a cone angle (θ) as described in Figure 3.21a[23] of which values are extracted from the high-magnification SEM images. Figure 3.21b shows the potential dependence of R and θ. The R of the Au tips prepared at 1.1 V was 1.6 ± 0.1 μm, which is much larger than that of conventional Au tips applied to TERS.[8-11] When the applied potential is 1.2 V, the sharp tips with small R (50.5 ± 18.7 nm) was obtained. The sharpest tips were available

at 1.3 V (R = 15.7 ± 2.5 nm). In contrast, the R obtained at 1.4 V is larger than that obtained at 1.3 V. This is because the competitive reactions between the dissolution and the oxide formation retard the flow of electrons. In addition, the bubbles formed at the Au surface would also affect the tip morphology. Therefore, R is well controlled by the applied potential. On the other hand, the values of θ obtained at 1.1-1.4 V are almost same and thus are not controlled by the applied potential (Figure 3.21b); it is influenced by the viscosity of the electrolyte solution, concentration of the electrolyte, thickness of electrical double layer on Au surfaces and so forth. However, it is difficult to identify the influential factor, because these factors would change the optimized etching potential.

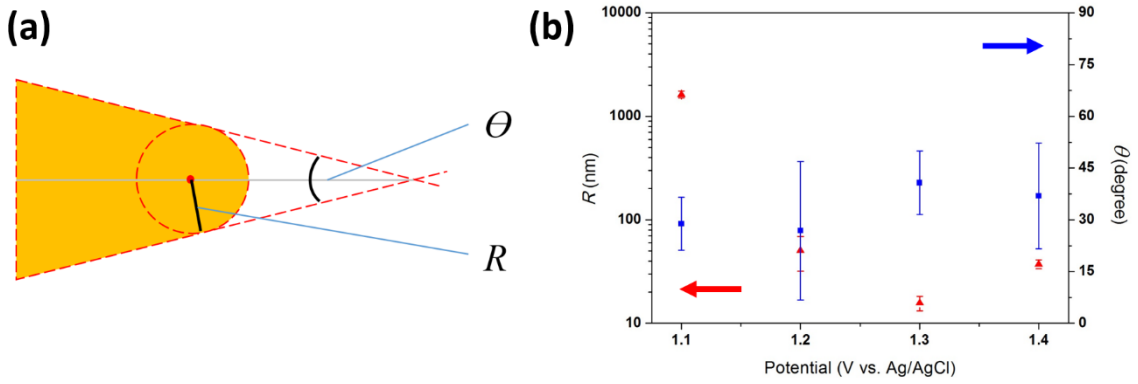

Figure 3.21. (a) The schematic model of the Au tip with a radius of curvature (R) and a cone angle (θ). (b) Applied potential dependence of R and θ. Each point is averaged from 6 tips.

To further supplement the Figure 3.21, all values of the R and θ of six tips prepared at 1.1 V, 1.2 V, 1.3 V, and 1.4 V are provided in Figures Figure 3.22 and Figure 3.23.

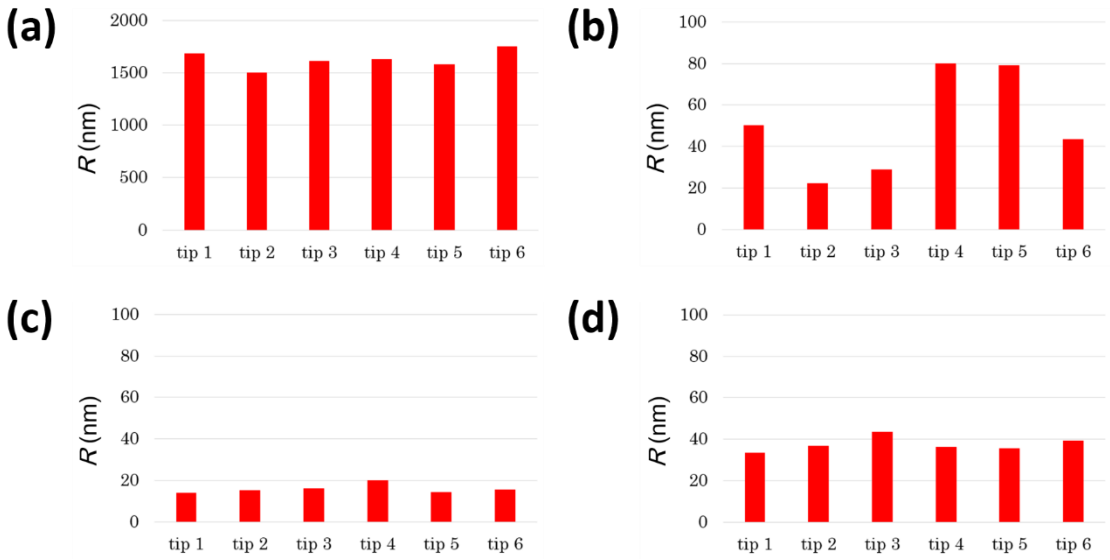

Figure 3.22. Radius of curvature (R) of Au tips prepared at different applied potentials. (a) 1.1 V, (b) 1.2 V, (c) 1.3 V, and (d) 1.4 V.

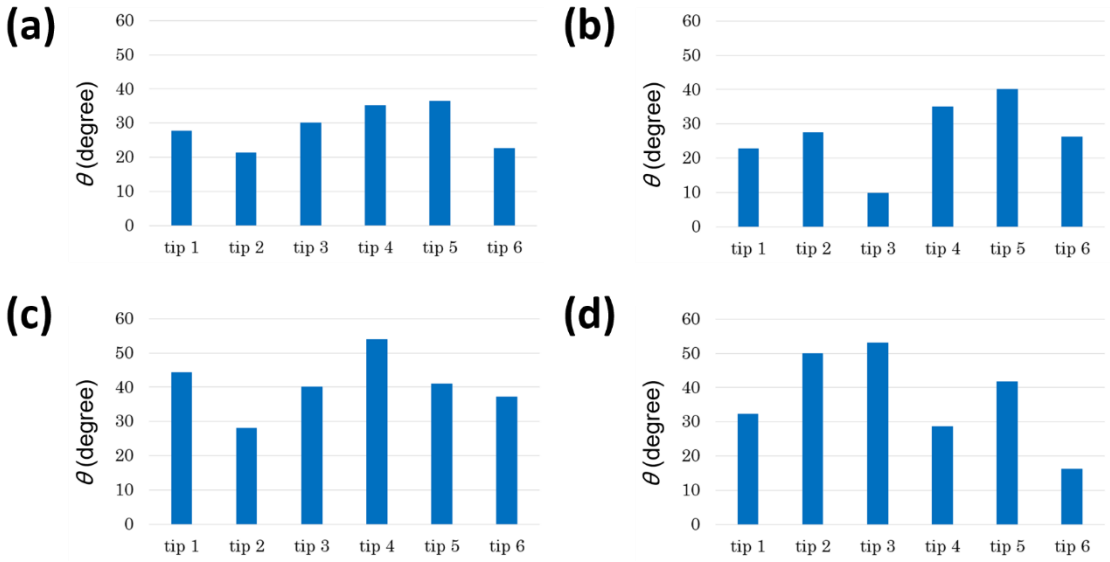

Figure 3.23. Cone angle (θ) of Au tips prepared at different applied potentials. (a) 1.1 V, (b) 1.2 V, (c) 1.3 V, and (d) 1.4 V.

3.3.5 Linear sweep voltammetry (LSV) measurements

The LSV measurements were performed before and after the fabrication of Au tips, for both the two- and three-electrode electrochemical etching systems to evaluate the stability of the applied system. The LSV curves were obtained with fresh Au wires which were not used for tip making. The LSV measurement and the tip making process were performed in turn. The initial and end points of the potential sweep were 0 V (-0.4 V) and 3.5 V (1.5 V) with two- (three-) electrode electrochemical system. The sweep rate was set at 0.1 V/s. Other conditions such as the voltage source, the electrolyte and the counter electrode were totally same.

The high reproducibility of tips has been required for practical applications of TERS because it is directly related to the reproducibility of the tip-enhancement effect.[41,42] The good controllability of the tip shape would be mainly based on the high stability of the etching system leading to good reproducibility of the etching process. In order to examine the stability of the electrochemical etching conditions, LSV measurements were carried out, comparing between the three-electrode and the conventional two-electrode electrochemical etching systems (Figure 3.24). The LSV curve obtained in prior to tip making (Figure 3.24a-1st) is identical to the CV curve in the positive potential sweep at 0.1 V/s. After the first Au tip was prepared at 1.3 V with a fresh Au wire, the LSV curve was measured with the same electrolyte solution with a different fresh Au wire (Figure 3.24a-2nd). The LSV measurement and the tip making process were performed in turn. Both the shape and the potential range of the curve are almost identical even after the preparation of 9 tips. This indicates that the etching condition didn’t change largely during the tip fabrication process although both the wire of CE and the concentration of Au ions in

the electrolyte changed as shown in Figure 3.25. Note that the small differences among the peak heights are caused by the error of the immersed depths of the wire.

The same analysis was performed with the two-electrode electrochemical etching system in the potential region near the anodic peak (Figure 3.24b). Although the initial shape of the curve is similar to the curves obtained with three-electrode electrochemical system, a shoulder at ~2 V appears gradually after the fabrication of few tips. With etching reaction going, the concentration of Cl^- in electrolyte solution gradually decreases, thus less amount of Cl^- are provided and more electrons are needed to keep the etching reaction. Furthermore, the successive potential shift of the anodic peak was observed. $U_{interface}$ (voltage between the CE and etching position) is kept as constant in the etching process; with the increase of "*IR*" (etching potential), U_{out} (applied potential) increases accordingly. So the potential shifts to the more positive direction. Thus, the weak point of two-electrode system is fluctuation of the electrochemical potential, which makes instability in the etching condition. In other words, the preparation of the Au tips with two-electrode electrochemical etching system has a critical problem about both stability and reproducibility, which deteriorates the controllability of the tip shape. In contrast, the three-electrode electrochemical etching system exhibits high stability leading to good reproducibility because of the electrochemical potential well controlled against RE.

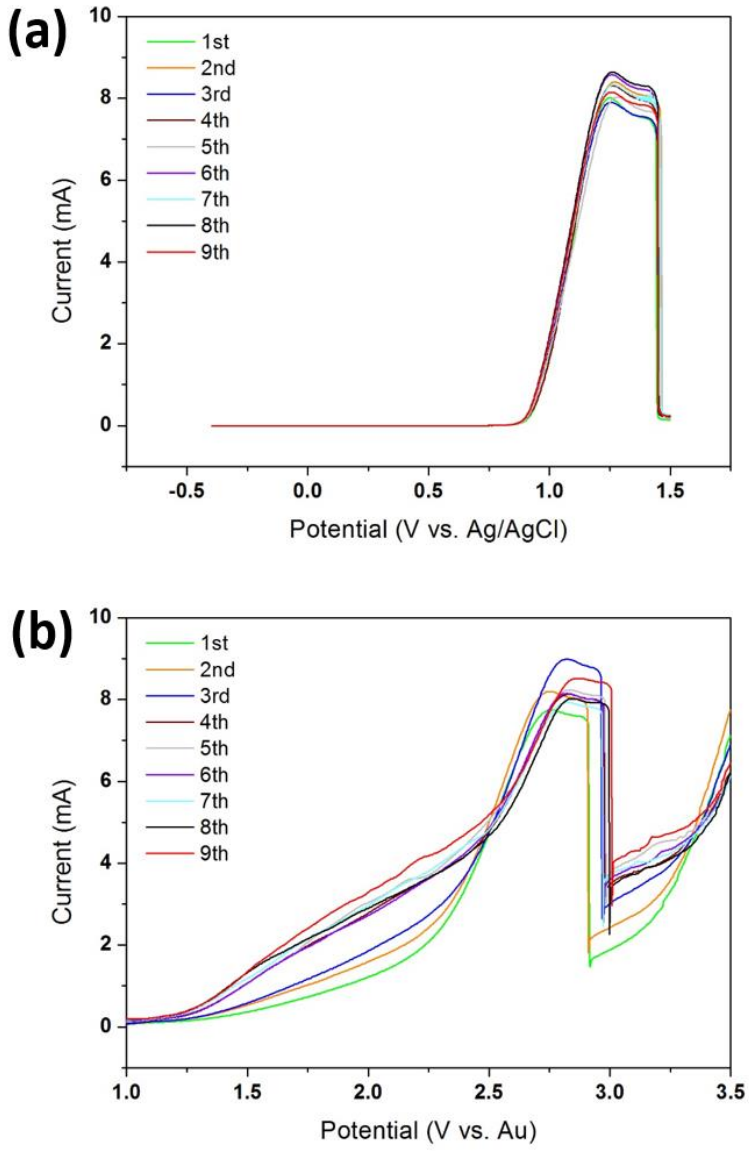

Figure 3.24. LSV curves in the positive potential sweep obtained with the (a) three- and (b) two-electrode electrochemical etching systems in the same electrolyte solution. The curves were measured with fresh Au wires before and after the fabrication of tips. The 1st curve was obtained in prior to tip making. The 2nd curve was measured after the first Au tip was prepared at 1.3 V with a fresh Au wire. The LSV measurement and the tip making were performed in turn. Scan rate is 0.1 V/s.

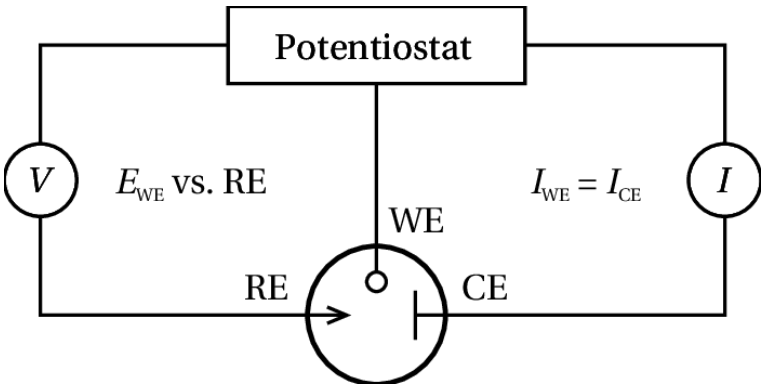

Figure 3.25. A brief structure diagram of the three-electrode electrochemical etching system.

For the three-electrode system, the Ag/AgCl reference electrode was then replaced with an Au reference electrode and the same LSV measurement was carried out (Figure 3.26). The overall trend is similar to the 3-electrode system case above (Figure 3.25a). The concentration of Cl^- gradually decreases with etching going and there's no supplementary source, so the measured anodic potential slightly shifted.

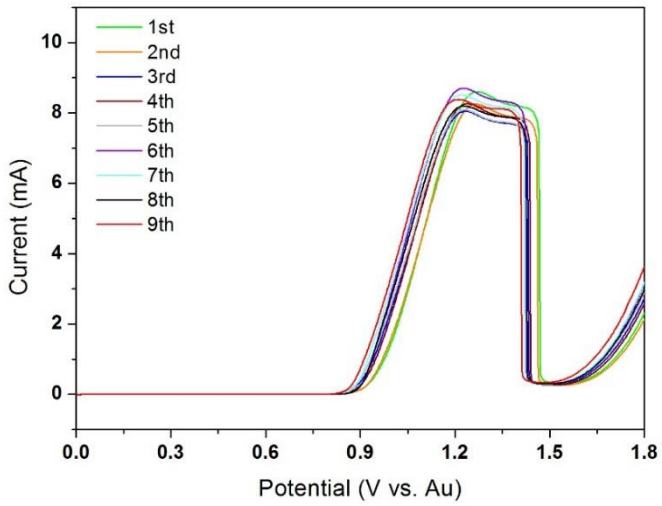

Figure 3.26. LSV curves in the positive potential sweep obtained with the three-electrode electrochemical etching systems with Au reference electrode.

We took pictures of some parts before and after our tip making experiment, and found some interesting phenomena. The new counter electrode (CE) made of a Au ring has smooth surface with metallic luster. However, the ring becomes dark after the fabrications of several tips, which is caused by the Au oxides on the surface of CE (Fig. 3.27b). The yellow color of the electrolyte solution results from the Au ions produced during the etching process.

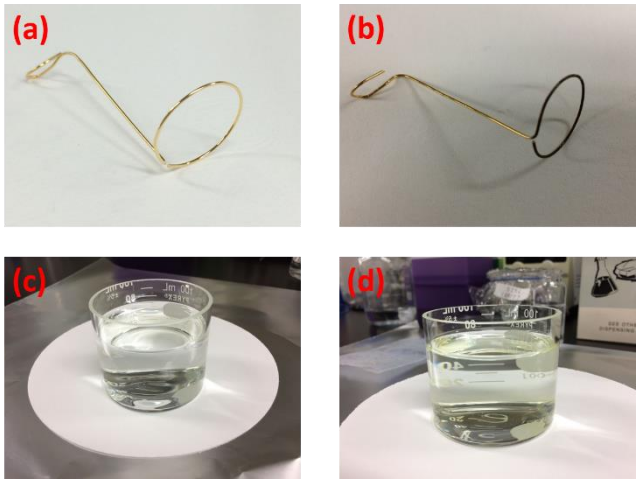

Figure 3.27. The pictures of the Au counter electrode (a) before and (b) after tip making, respectively. The pictures of the KCl electrolyte solution (c) before and (b) after tip making, respectively.

3.4 Conclusions

We fabricated Au tips with high reproducibility and controllability by electrochemical etching at a constant anodic potential in a KCl aqueous solution with a three-electrode electrochemical etching system. The curvature of radius was controlled by the applied potential. The electrochemical analysis revealed that the stability of the three-electrode

electrochemical etching system is much higher than that of the conventional two-electrode electrochemical etching system. The Au tips with the sharpness obtained at 1.3 V would be applicable not only as STM tips with high spatial resolution but also as probes exhibiting strong field enhancement in TERS.

3.5 References

1. Baykul, M. C. *Mater. Sci. Eng.: B* **2000**, *74*, 229.

2. Olson, J. A.; Bühlmann, P. *Anal. Chem.* **2003**, *75*, 1089.

3. Ren, B.; Picardi, G.; Pettinger, B. *Rev. Sci. Instrum.* **2004**, *75*, 837.

4. Gingery, D.; Bühlmann, P. *Rev. Sci. Instrum.* **2007**, *78*, 113703.

5. Tuchband, M.; He, J.; Huang, S.; Lindsay, S. *Rev. Sci. Instrum.* **2012**, *83*, 015102.

6. Libioulle, L.; Houbion, Y.; Gilles, J. M. *J. Vac. Sci. Technol. B* **1995**, *13*, 1325.

7. Nam, A. J.; Teren, A.; Lusby, T. A.; Melmed, A. J. *J. Vac. Sci. Technol. B* **1995**, *13*, 1556.

8. Wang, X.; Liu, Z.; Zhuang, M. D.; Zhang, H. M.; Wang, X.; Xie, Z. X.; Wu, D. Y.; Ren, B.; Tian, Z. Q. *Appl. Phys. Lett.* **2007**, *91*, 101105.

9. Williams, C.; Roy, D. *J. Vac. Sci. Technol. B* **2008**, *26*, 1761.

10. Lopes, M.; Toury, T.; de la Chapelle, M. L.; Bonaccorso, F.; Gucciardi, P. G. *Rev. Sci. Instrum.* **2013**, *84*, 073702.

11. Xu, G. Z.; Liu, Z. H.; Xu, K.; Zhang, Y.; Zhong, H. J.; Fan, Y. M.; Huang, Z. L. *Rev. Sci. Instrum.* **2012**, *83*, 103708.

12. Roy, D.; Williams, C. M.; Mingard, K. *J. Vac. Sci. Technol. B* **2010**, *28*, 631.

13. Lee, C.; Kim, S. T.; Jeong, B. G.; Yun, S. J.; Song, Y. J.; Lee, Y. H.; Park, D. J.; Jeong, M. S. *Sci. Rep.* **2017**, *7*, 40810.

14. Xiao. L.; Schultz, Z. D. *Anal. Chem.* **2018**, *90*, 440.

15. Bonhommeau, S.; Lecomte, S. *Chem. Phys. Chem.* **2018**, *19*, 8.

16. Billot, L.; Berguiga, L.; de la Chapellea, M. L.; Gilbert, Y.; Bachelot, R. *Eur. Phys. J. Appl. Phys.* **2005**, *31*, 139.

17. Eligal, L.; Culfaz, F.; McCaughan, V.; I. Cade, N.; Richards, D. *Rev. Sci. Instrum.* **2009**, *80*, 033701.

18. Eisele, M.; Krüger, M.; Schenk, M.; Ziegler, A.; Hommelhoff, P. *Rev. Sci. Instrum.* **2011**, *82*, 026101.

19. Sergey, S. K.; Alexey, I. N.; Günter, G. H.; Joachim, L. *Nanotech*. **2011**, *22*, 025202.

20. Abadal, G.; Pérez-M., F.; Barniol, N.; Aymerich, X. *IEEE Trans. Instrum. Meas.* **2003**, *52*, 859.

21. Narasiwodeyar, S.; Dwyer, M.; Liu, M.; Park, W. K.; Greene, L. H. *Rev. Sci. Instrum.* **2015**, *86*, 033903.

22. Mayer, K. M.; Hafner, J. H. *Chem. Rev.* **2011**, *111*, 3828.

23. Huang, T. X.; Huang, S. C.; Li, M. H.; Zeng, Z. C.; Wang, X.; Ren, B. *Anal. Bioanal. Chem.* **2015**, *407*, 8177.

24. Klein, M.; Schwitzgebel, G. *Rev. Sci. Instrum.* **1997**, *68*, 3099.

25. John, L. V.; Werner, K. *Thin Film Processes*. Academic, New York, **1978**.

26. Burke, M. G.; Sieloff, D. D.; Brenner, S. S. *J. Phys. (Paris)*. **1986**, *47-C7*, 459.

27. Müller, E. W. *Z. Physik.* **1937**, *106*, 132.

28. Gomer, R. *J. Chem. Phys.* **1958**, *28*, 457.

29. Melmed, A. J.; Gomer, R. *J. Chem. Phys.* **1959**, *30*, 586.

30. Melmed, A. J. *J. Chem. Phys.* **1963**, *38*, 607.

31. Hibi, T. *J. Electronmicr.* **1956**, *4*, 10.

32. Hibi, T.; Ishikawa, K. *Sci. Rept. Res. Inst. Tohoku Univ.* **1961**, *13*, 311.

33. Binnig, G.; Rohrer, H.; Gerber, Ch.; Weibel, E. *Phys. Rev. Lett.* **1982**, *49*, 57.

34. Murphy, C. J.; Jana, N. R. *Adv. Mater.* **2002**, *14*, 80.

35. Stephan, L.; Mostafa, A. E. *J. Phys. Chem. B* **1999**, *103*, 8410.

36. Kelly, K. L.; Coronado. E.; Zhao, L. L.; Schatz, G. C. *J. Phys. Chem. B* **2003**, *107*, 668.

37. Demming, A. L.; Festy F.; Richards, D. *J. Chem. Phys.***2005**, *122*, 18.

38. Yang, Z. L.; Aizpurua, J.; Xu, H. X. *J. Raman Spectrosc.* **2009**, *40*, 1343.

39. Angulo, A. M.; Noguez, C.; Schatz, G. C. *J. Phys. Chem. Lett.* **2011**, *2*, 1978.

40. Ye, S.; Ishibashi, C.; Shimazu, K.; Uosaki, K. *J. Electrochem. Soc.* **1998**, *145*, 1614.

41. Johnson, T. W.; Lapin, Z. J.; Beams, R.; Lindquist, N. C.; Rodrigo, S. G.; Lukas Novotny, L.; Oh, S. H. *ACS Nano* **2012**, *6*, 9168.

42. Hayazawa, N.; Yano, T.; Kawata, S. *J. Raman Spectrosc.* **2012**, *43*, 1177.

Chapter 4

Single molecular STM study

4.1 Introduction

Studies of single-molecule reactions on surfaces using STM provide unprecedented insight into the structure of reactants and products, as well as the reaction pathways.[1-4] Photo-induced dissociation is one of the important applications of solar energy. Nevertheless, it is infeasible to realize this reaction for the small molecules in gas and liquid phases because of the wide energy gap between frontier molecular orbitals, such as highest occupied molecular orbital (HOMO) and lowest unoccupied molecular orbital (LUMO).[5] UV light-induced molecular photochemistry on single-crystalline metal surfaces has been widely studied.[6-14]

Two excitation mechanisms were proposed for the UV light-induced surface dynamics of adsorbates on metal surfaces, as shown in Figure 4.1.[5] In the indirect excitation (Figure 4.1a), hot electrons generated in a bulk metal transiently enter the unoccupied states of the adsorbates through an inelastic scattering process, determined by the density of hot electrons in the metal substrate.[13] This is the primary pathway of photochemical reactions on metal surface, and only a few experimental observations belong to direct mechanism.[6,8,10-12] Photo-induced dissociation via direct excitation of the frontier electronic states of an adsorbate on a metal substrate has been reported for physisorbed (Figure 4.1b) and chemisorbed molecules (Figure 4.1c).

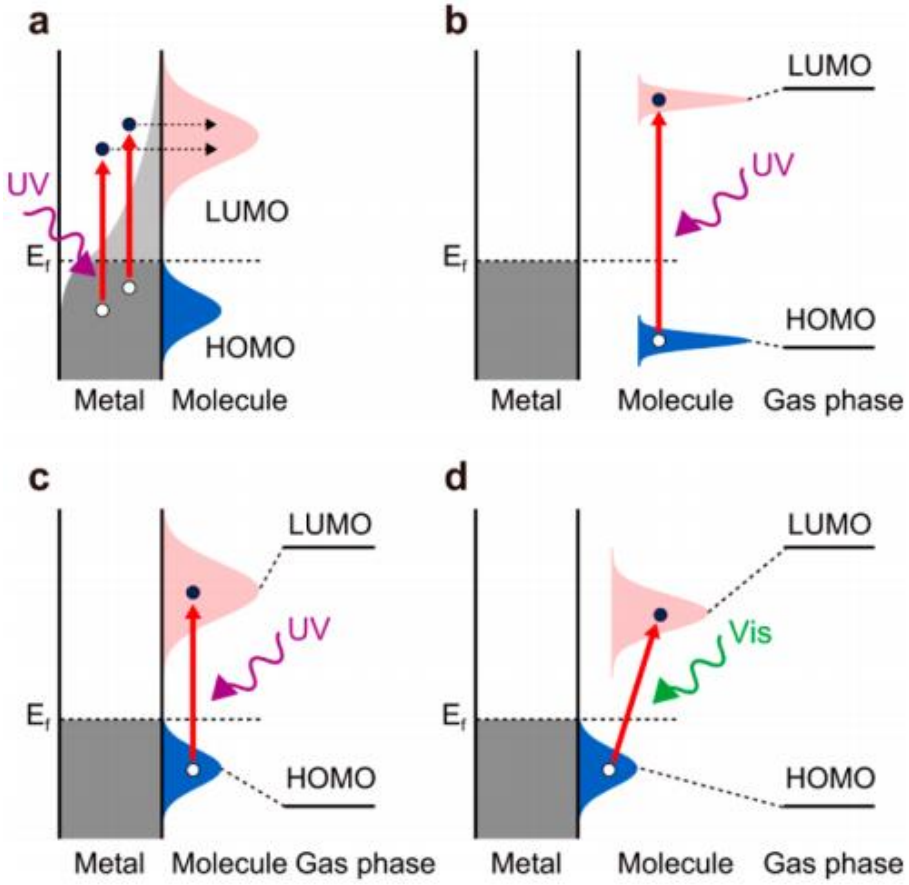

Figure 4.1. (a−c) Excitation mechanisms of UV-induced reactions on metal surfaces. The light gray area illustrates the energy distribution of hot electrons. (d) Excitation mechanism of visible light-induced dissociation on metal surfaces. Reproduced with permission from ref. 5.

Molecule−surface interaction results in the reconstruction of interfacial electronic structures. Consequently, a new opportunity for chemical reactions with visible light can be provided by molecular adsorption on solid surfaces. Visible light-induced dissociation using both plasmonic noble metal[15-17] and non-plasmonic transition metal[18,19] nanoparticles has been achieved. Atomically well-defined surfaces of metal single crystals allows

us to investigate the photo-induced surface dynamics and the changes in electronic structure.[20-22]

In this chapter, I report plasmon-induced dissociation of dimethyl disulfide (DMDS) on Au(111) surface. Localized surface plasmon is excited by visible light as described in chapter 3. Figure 4.2 shows a schematic of my experimental set-up. A quantitative analysis of the STM images revealed that S−S bond dissociation was induced by the plasmon under visible-light irradiation.[23-30] Hybridization between the molecule and metal reduces the energy gap between the frontier molecular electronic states derived from the HOMO and LUMO of DMDS in the gas phase, resulting in an energy gap accessible with visible light.[5] Particularly, the LUMO-derived MOs overlap with the metal surface and so lifetime of the photo-excited state becomes long enough to induce dissociation (Figure 4.1d).

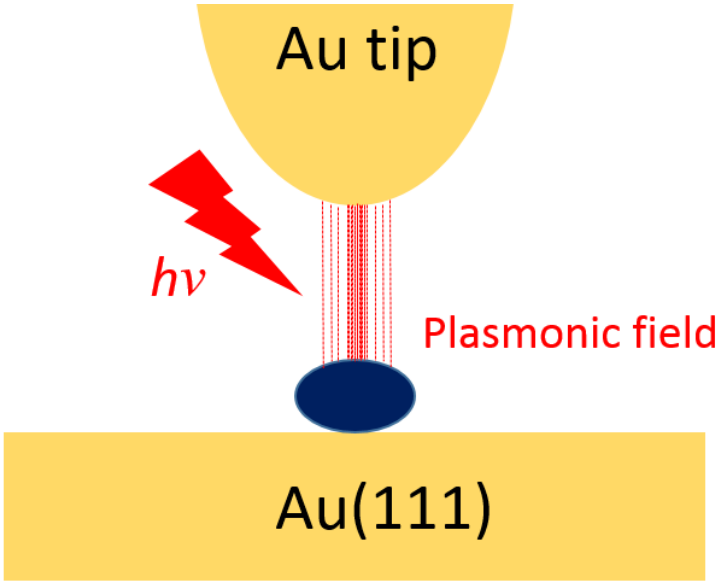

Figure 4.2. Schematic of plasmon-induced dissociation of a single molecule on Au(111) substrate with an Au tip.

Previous STM studies revealed the tunneling electron-induced dissociation of adsorbed

molecules on noble metal surface.[31-33] As for a single DMDS molecule, dissociation reactions occurred on Au(111) surface with a W tip.[34] Figure 4.3 shows the STM images before and after dissociation of DMDS molecules reported by J. Yates's group. The dissociation likely occurs via electronic excitation of the molecule due to the relatively high threshold energy (~1.4 V). Surprisingly, the *trans*-conformation of the parent DMDS molecule is often reflected in the relative position and alignment of two product CH_3S species, which are grouped into *trans*-pairs. The orientation of the DMDS molecule on the surface (the direction of its S-S bond) is also retained in dissociation because the *trans*-pairs are related to each other by the same symmetry operations as their parent DMDS molecules.

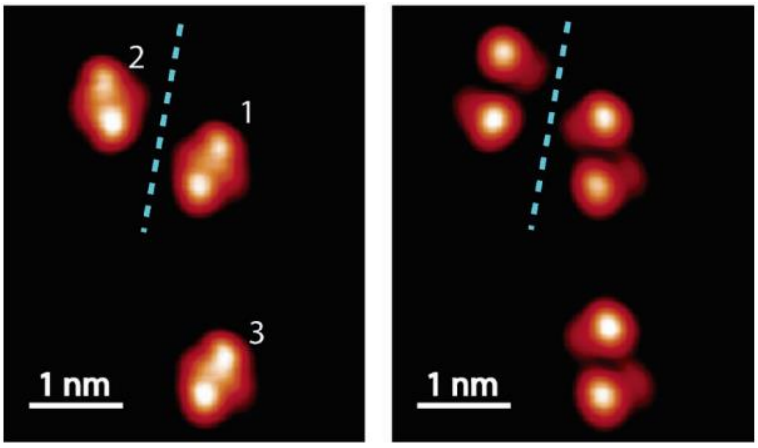

Figure 4.3. Electron-induced dissociation of DMDS molecules on the Au(111) surface as seen by STM. The products retain the conformation and orientation of the parent molecules: molecules 1 and 3 are identical, producing identical CH_3S trans-pairs. Molecules 1 and 2 are offset mirror images of each other, and so are the product trans-pairs of CH_3S species (dashed blue line is the mirror plane). Reproduced with permission from ref. 34. Figure 4.4 indicates the schematics before and after dissociation.

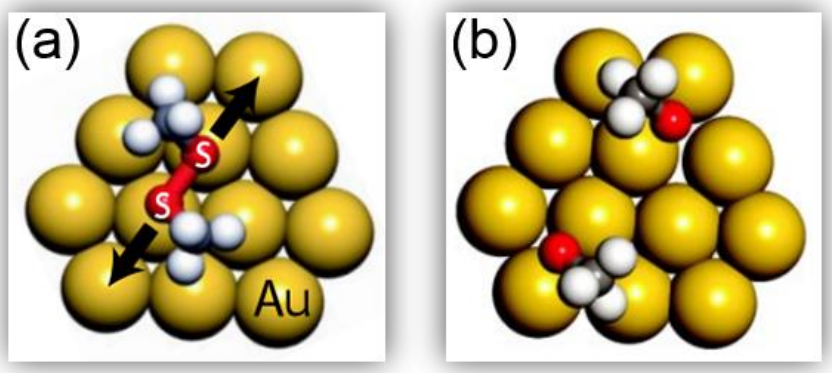

Figure 4.4. Models of (a) DMDS molecule on the Au(111) surface and (b) the two CH_3S products after electron-induced dissociation. Reproduced with permission from ref. 35.

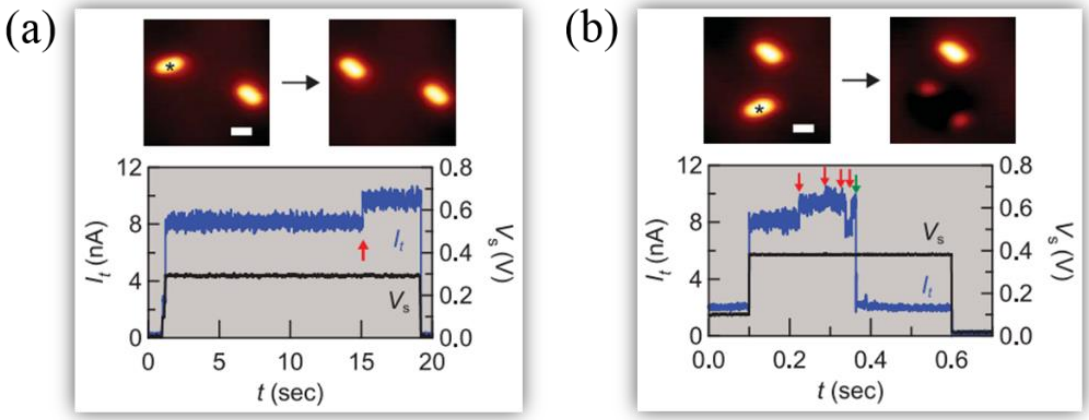

Figure 4.5. STM images and current traces of tunneling electron-induced reactions on Ag(111) with a Ag tip. The tunneling conditions are (a) V_s = 0.30 V, I_t = 8.0 nA, and (b) V_s = 0.38 V, I_t = 8.0 nA. The current changes indicated by red and green arrows correspond to rotation and dissociation, respectively. The black star indicates tip position. The scale bars in the STM images are 0.5 nm. Reproduced with permission from ref. 36.

Most recently, Kazuma *et al.* found both rotation (Figure 4.5a) and dissociation (Figure

4.5b) occurred on Ag(111) surface with W tip through vibrational excitation of inelastically tunneled electrons.[36] What's more, dissociation induced with tunneling electrons was accompanied by rotation, which results in small changes in I_t followed by its sudden drop.

4.2 Experimental

4.2.1 Plasmon-induced dissociation of a DMDS molecule

All the measurements were carried out at 5.0 K with a low-temperature STM (Omicron GmbH) under ultrahigh vacuum below 5.0×10^{-11} Torr. The Au(111) surface was cleaned by several cycles of Ar^+-ion sputtering and annealing at ~660˚C. The adsorbate molecules (DMDS) were deposited by evaporation from a glass ampule at room temperature. The temperature of the substrate was <50 K. Scanning conditions for obtaining STM images were V_s = 30 mV, I_t = 0.2 nA. To generate plasmon, Au tips were used for this experiment.

The light was p-polarized and introduced into the STM chamber through a view port (transmittance ≥95% at 365−1000 nm) with an incident angle of 25°to the sample surface. The light was collected by lenses outside of the chamber and concentrated on the sample surface with a spot diameter of ~1.2 mm. The visible light sources was a Xe lamp (Laser Driven Light Source, TOKYO INSTRUMENTS, INC) equipped with 670 nm bandpass filter (fwhm = 10 nm, THORLABS). The light intensity was tuned with an ND filter (THORLABS) and was evaluated with an optical power meter (THORLABS) and a dual scanning slit beam profiler (THORLABS).

4.2.2 Tunneling electron-induced dissociation of a single DMDS molecule

All the measurements were carried out at 5.0 K with a low-temperature STM (Omicron GmbH) under ultrahigh vacuum below 5.0×10^{-11} Torr. The Au(111) surface was cleaned by several cycles of Ar^{+}-ion sputtering and annealing at ~660˚C. The adsorbate molecules (DMDS) were deposited by evaporation from a glass ampule at room temperature. The temperature of the substrate was <50 K. Scanning conditions for obtaining STM images were V_s = 30 mV, I_t = 0.2 nA. A tungsten (W) tip is used during the whole measurements.

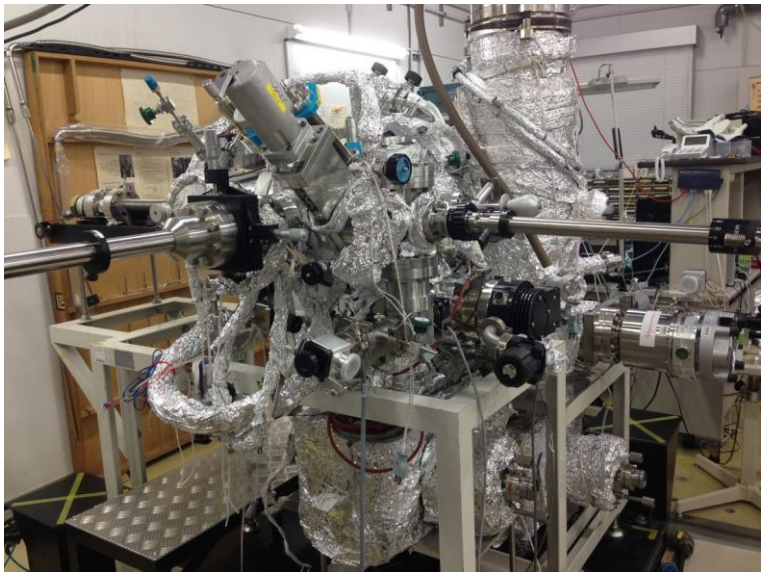

Figure 4.6. A picture of our scanning tunneling microscopy

4.3 Results and Discussion

First of all, STM imaging of the Au(111) surface was carried out. We applied different bias voltages (-3 V, -2 V, -1 V, 1 V, 2 V, and 3 V) and the results were shown in Figure 4.7. The typical herringbone reconstructions of Au(111) can be seen clearly, indicating

that the Au tips are available and stable.

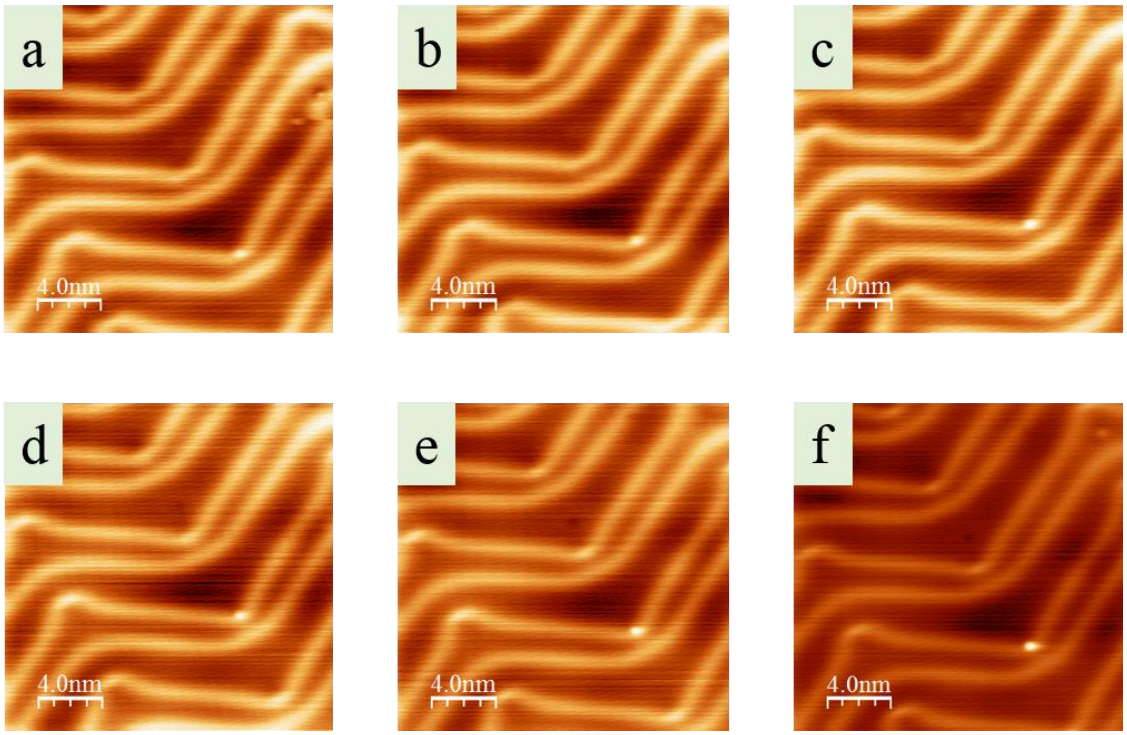

Figure 4.7. STM images of the Au(111) surface at different bias voltages. (a) -3 V, (b) -2 V, (c) -1 V, (d) 1 V, (e) 2 V, and (f) 3 V. The tunneling current is fixed at 1 nA.

After the target molecules were deposited, we tried to obtain the STM image again. From the result in Figure 4.8, the light spots are the DMDS molecules, mainly located at the spaces among the herringbones. The lightest spots are the molecular clusters, and the medium light spots may be dimers.

To obtain high resolution STM images, the atomic apex of the tip is more important than geometrical parameters of R and θ. In the case of conventional tungsten tips, the cleaning process by applying high bias voltage pulse to remove oxide and contaminations on tip surface is necessary to obtain high resolution STM images. This cleaning process changes not only atomic apex but also geometrical shape of the tip such as R. In contrast,

our Au tips with smooth surfaces are chemically stable and hardly deteriorate due to contamination. Thus, our Au tips are expected to be used as stable plasmonic tips without shape changes caused by applying high bias voltage.

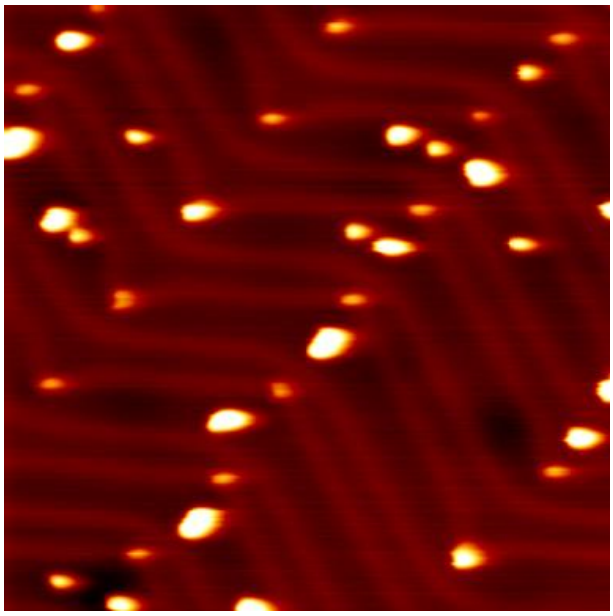

Figure 4.8. A typical STM image of the DMDS molecules on Au(111) surface. The scanning condition is V_s = 30 mV, I_t = 0.2 nA.

Based on the work above, now we can carry out the trial of plasmon-induced dissociation of the same molecule. After duration of 1 minute with the visible light pulse (670 nm, 2.64 mW), the dissociation of a single molecule occurred; then we repeated the same excitation and after 5 minutes, the second plasmon-induced dissociation reaction occurred (Figure 4.9). With regard to the mechanism, we already discussed in the Introduction part: hybridization between the molecule and metal reduces the energy gap between the frontier molecular electronic states derived from the HOMO and LUMO of DMDS in the gas phase, resulting in an energy gap accessible with visible light. The LUMO-derived MOs overlap with the metal surface and so lifetime of the photo-excited state becomes long

enough to induce dissociation (Figure 4.1d).

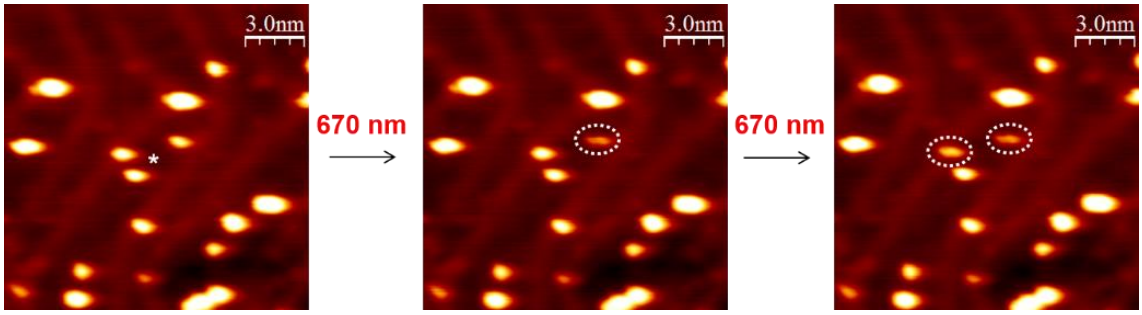

Figure 4.9. Plasom-induced dissociation of a single DMDS molecule on Au(111) surface. The excitation source is visible light with wavelength of 670 nm. The white star indicates tip position. Dot circles indicate the dissociated molecules.

We can estimate the range of plasmonic field by some skills. Dr. Kazuma and her collaborators analyzed plasmonic field, by division of the STM image into four areas (Figure 12a). Then they obtained the time dependence of the dissociation ratio by statistics. The value for Area 4 is almost zero which indicates that there's almost no reactions in this region.

Now go back to my case, there are three molecules in the surrounding of the STM tip. But only two of then finally dissociated under the irradiation of the 670 nm visible light. So the size of the plasmonic field is almost equivalent to the horizontal distance of the molecule and the tip. It is about a circle with diameter of 3 nm and the center is the point of Au(111) surface that the tip right pointed. This is not so accurate because of lack of systematic data.

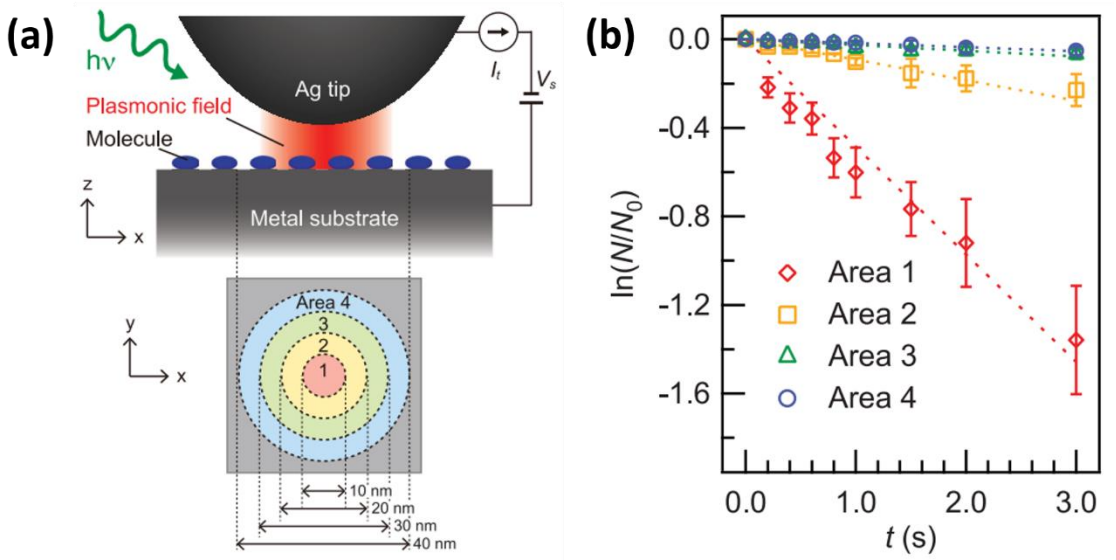

Figure 4.10. Real-space investigations of the plasmon-induced chemical reaction. (a) Schematic illustration of the experiment for the real-space investigation of the plasmon-induced chemical reaction in the nanogap between a Ag tip and a metal substrate, and division of the STM image into four areas depicted with 10-nm wide concentric rings for analysis. (b) Time dependence of the dissociation ratio (N/N_0) under irradiation with p-polarized light at 532 nm in the four areas shown in (a). Reproduced with permission from ref. 36.

Figure 4.11 demonstrates the process of electron-induced dissociation of a single DMDS molecule. Under the pulse of V_e = 0.8 V, and I_e = 0.25 nA, the position of target molecule had no change (Figure 4.11a). After a pulse of V_e = 0.9 V, and I_e = 0.2222 nA, the rotation reaction occurred but not dissociated (Figure 4.11b). Then we further increased the bias voltage to 1.0 V (current of 0.2 nA), and the dissociation reaction occurred (Figure 4.11c).

To explore the dissociation mechanism, we fixed the current at 40 nA. Then the bias voltage is gradually increasing from zero, and we found the target molecule kept stable

until 0.35 V. After the pulse of 0.36 V, dissociation reaction occurred (Figure 4.12b). So the threshold energy is 0.36 V, which corresponds to the energy of C-H stretching vibration mode, reported for the monolayer of DMDS on Au(111).[37]

J. Yates group reported that the threshold energy of dissociation of S-S bond in DMDS on Au(111) surface was ~1.4 V. The tunneling current they applied was 20 pA, which was too small to find a real threshold energy. Thus, I conclude that the dissociation of DMDS on Au(111) is induced via vibrational excitation by injecting tunneling electrons at ≥ 0.36 V.

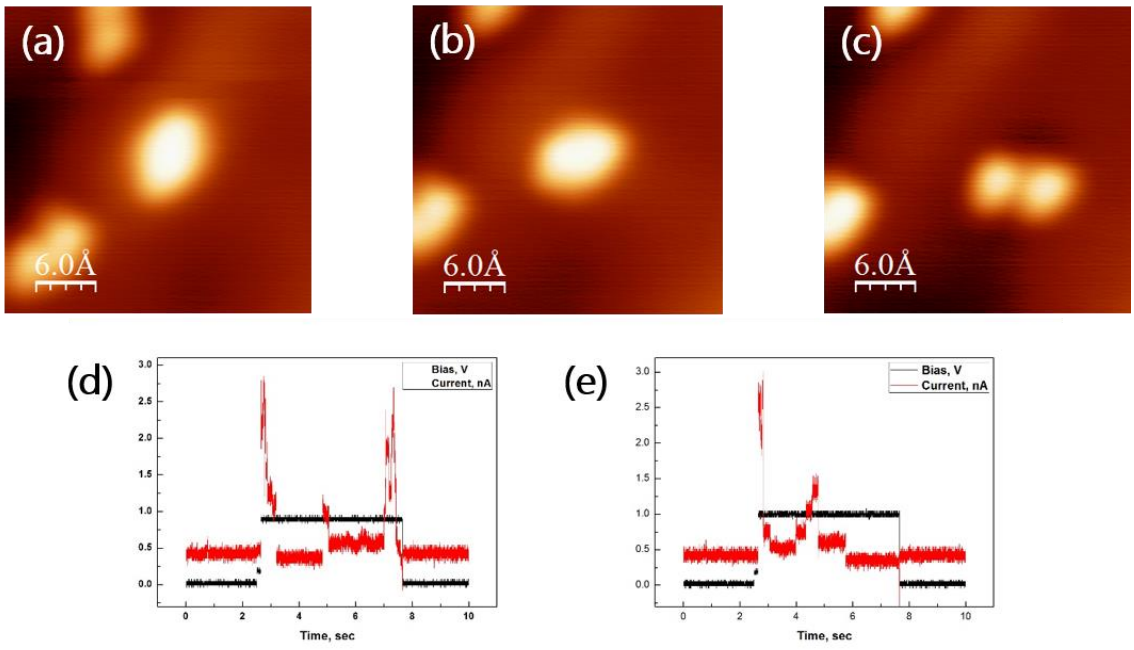

Figure 4.11. Tunneling electron-induced dissociation of a single DMDS molecule on Au(111) surface with a W tip. (a-c) and (d, e) are the STM images and the corresponding current traces, respectively. The excitation conditions are (a) V_e = 0.8 V, I_e = 0.25 nA, (b) V_e = 0.9 V, I_e = 0.2222 nA and (c) V_e = 1.0 V, I_e = 0.2 nA.

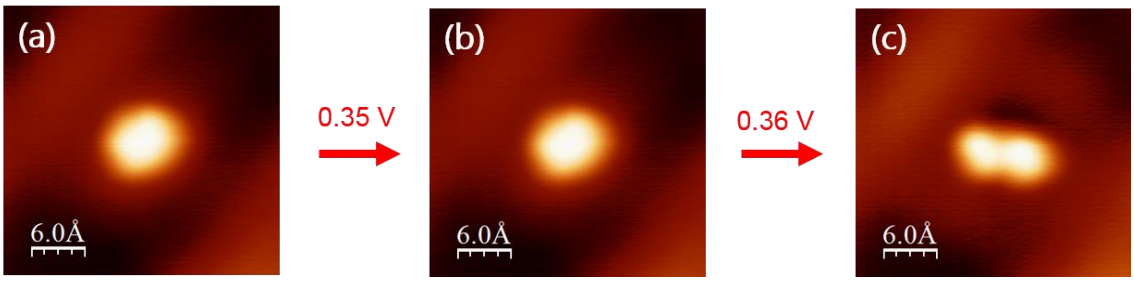

Figure 4.12. Mechanism exploration of tunneling electron-induced dissociation at a fixed current of 40 nA. The bias voltages are 0.35 V (a-b) and 0.36 V (b-c).

In addition, independent rotation and desorption reactions were also found at threshold energy (Figure 4.13). The recorded current trace can be a powerful proof. As seen from Figure 4.13a, the current is continuously fluctuating during the bias pulse, indicating the target molecule is rotating in the whole process. In comparison, the current fluctuation terminated during the pulse because the molecule has already desorbed at that time.

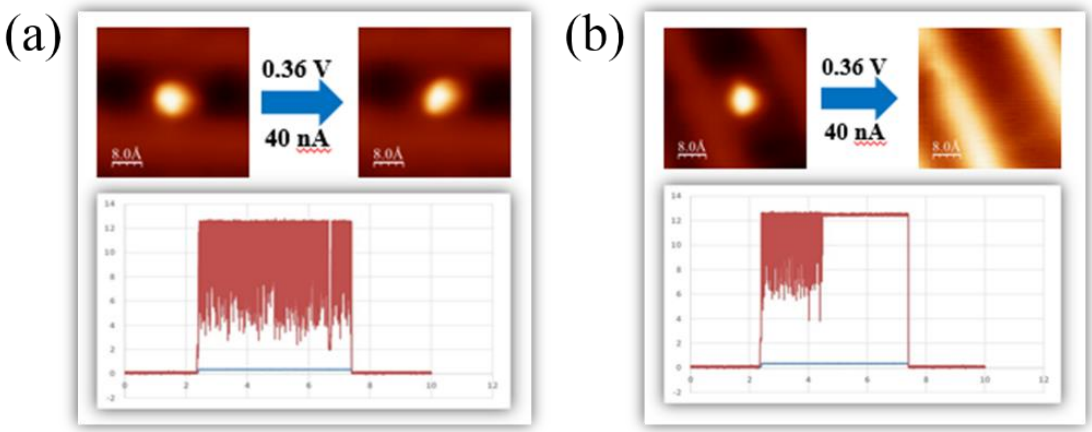

Figure 4.13. STM images before and after (a) rotation and (b) desorption reactions at the threshold energy of 0.36 V. The lower part indicates the current trace during excitation. The current was fixed at 40 nA.

4.4 Conclusions

Plasmon-induced reaction of a single DMDS molecule on Au(111) with a Au tip was carried out with a 670 nm-visible light. Dissociation reaction successfully occurred. Any molecular motion such as rotation, translation and desorption was not observed. Tunneling electron-induced reaction of the same molecule on the same substrate with a W tip was investigated. Three reactions of dissociation, rotation and desorption were found.

Table 4.2 Plasmon-induced and tunneling electron-induced reactions of a single DMDS molecule on different substrate with different tip.

Plasmon-induced reaction	**Electron-induced reaction**
Ag tip on Ag(111) Only dissociation	W tip on Ag(111) Rotation + Dissociation
Au tip on Au(111) Only dissociation	W tip on Au(111) Rotation + Dissociation + Desorption

4.5 References

1. Tsai, C.-S.; Wang, J.-K.; Skodje, R. T.; Lin, J.-C. *J. Am. Chem. Soc.* **2005**, *127*, 10788.

2. Hossain, Md. Z.; Kato, H. S.; Kawai, M. *J. Am. Chem. Soc.* **2005**, *127*, 15030.

3. Henzl, J.; Mehlhorn, M.; Gawronski, H.; Rieder, K.-H.; Morgenstern, K. *Angew. Chem., Int. Ed*. **2006**, *45*, 603.

4. Lastapis, M.; Martin, M.; Riedel, D.; Hellner, L.; Comtet, G.; Dujardin, G. *Science* **2005**, *308*, 1000.

5. Kazuma, E.; Jung, J.; Ueba, H.; Trenary, M.; Kim, Y. *J. Am. Chem. Soc*. **2017**, *139*,

3115.

6. Zhu, X. Y.; Hatch, S. R.; Campion, A.; White, J. M. *J. Chem. Phys.* **1989**, *91*, 5011.

7. Hatch, S. R.; Zhu, X. Y.; White, J. M.; Campion, A. *J. Phys. Chem.* **1991**, *95*, 1759.

8. Zhou, X. − L.; White, J. M. *J. Phys. Chem.* **1990**, *94*, 2643.

9. Kidd, R. T.; Lennon, D.; Meech, S. R. *J. Phys. Chem. B* **1999**, *103*, 7480.

10. Ying, Z. C.; Ho, W. *J. Chem. Phys.* **1991**, *94*, 5701.

11. Petek, H.; Weida, M. J.; Nagano, H.; Ogawa, S. *Science* **2000**, *288*, 1402.

12. Wolf, M.; Hotzel, A.; Knoesel, E.; Velic, D. *Phys. Rev. B: Condens. Matter Mater. Phys.* **1999**, *59*, 5926.

13. Zhu, X. Y.; White, J. M.; Wolf, M.; Hasselbrink, E.; Ertl, G. *Chem. Phys. Lett.* **1991**, *176*, 459.

14. Liu, Z. M.; Costello, S. A.; Roop, B.; Coon, S. R.; Akhter, S.; White, J. M. *J. Phys. Chem.* **1989**, *93*, 7681.

15. Christopher, P.; Xin, H.; Marimuthu, A.; Linic, S. *Nat. Mater*. **2012**, *11*, 1044.

16. Mukherjee, S.; Zhou, L.; Goodman, A. M.; Large, N.; Zhang, Y.; Nordlander, P.; Halas, N. J.; Ayala-Orozco, C. *J. Am. Chem. Soc.* **2014**, *136*, 64.

17. Kale, M. J.; Avanesian, T.; Christopher, P. *ACS Catal.* **2014**, *4*, 116.

18. Sarina, S.; Zhu, H.; Xiao, Q.; Jaatinen, E.; Jia, J.; Huang, Y.; Zheng, Z.; Wu, H. *Angew. Chem. Int. Ed.* **2014**, *53*, 2935.

19. Kale, M. J.; Avanesian, T.; Xin, H. L.; Yan, J.; Christopher, P. *Nano Lett.* **2014**, *14*, 5405.

20. Bartels, L.; Wang, F.; Moller, D.; Knoesel, E.; Heinz, T. F. *Science* **2004**, *305*, 648.

21. Comstock, M. J.; Levy, N.; Kirakosian, A.; Cho, J.; Lauterwasser, F.; Harvey, J. H.; Strubbe, D. A.; Frechet, J. M. J.; Trauner, D.; Louie,´ S. G.; Crommie, M. F. *Phys. Rev.*

Lett. **2007**, *99*, 038301.

22. Bazarnik, M.; Henzl, J.; Czajka, R.; Morgenstern, K. *Chem. Commun.* **2011**, *47*, 7764.

23. Sheraton, D. F.; Murray, F. E. *Can. J. Chem.* **1981**, *59*, 2750.

24. Thompson, S. D.; Carroll, D. G.; Watson, F.; O'Donnell, M.; McGlynn, S. P. *J. Chem. Phys.* **1966**, *45*, 1367.

25. Bao, S.; Mcconville, C. F.; Woodruff, D. P. *Surf. Sci.* **1987**, *187*, 133.

26. Boyd, D. B. *J. Am. Chem. Soc.* **1972**, *94*, 8799.

27. Lee, Y. R.; Chiu, C. L.; Lin, S. M. *J. Chem. Phys.* **1994**, *100*, 7376.

28. Rinker, A.; Halleman, C. D.; Wedlock, M. R. *Chem. Phys. Lett.* **2005**, *414*, 505.

29. Luo, C.; Du, W.; Duan, X.; Liu, J.; Li, Z. *Chem. Phys. Lett.* **2009**, *469*, 242.

30. Martínez-Haya, B.; Bass, M. J.; Brouard, M.; Vallance, C.; Torres, I.; Barr, J. *J. Chem. Phys.* **2004**, *120*, 11042.

31. Ho, W. *J. Chem. Phys.* **2002**, *117*, 11033.

32. Lu, P. H.; Polanyi, J. C.; Rogers, D. *J. Chem. Phys.* **1999**, *111*, 9905.

33. Sloan, P. A.; Palmer, R. E. *Nature* **2005**, *434*, 367.

34. Peter, M.; John T. Y. *J. Am. Chem. Soc.* **2006**, *128*, 10642.

35. Peter, M.; Daniel, B. D.; Zhu, X.-Y.; John T. Y. *Phys. Rev. Lett.* **2007**, *99*, 016101.

36. Kazuma, E.; Jung, J.; Ueba, H.; Trenary, M.; Kim, Y. *Science* **2018**, *360*, 521.

37. Nuzzo, R. G.; Zegarski, B. R.; Dubois, L. H. *J. Am. Chem. Soc.* **1987**, *109*, 733.

Chapter 5

Conclusions and outlook

Sharp Au tips were fabricated with high reproducibility and controllability by electrochemical etching at a constant anodic potential in a KCl aqueous solution with a three-electrode electrochemical etching system. The curvature of radius was controlled by the applied potential. The electrochemical analysis revealed that the stability of the three-electrode electrochemical etching system is much higher than that of the conventional two-electrode electrochemical etching system. The Au tips with the sharpness obtained at 1.3 V would be applicable not only as STM tips with high spatial resolution but also as probes exhibiting strong field enhancement in TERS.

Plasmon-induced reaction of a single DMDS molecule on Au(111) with a Au tip was carried out with a 670 nm-visible light. Dissociation reaction successfully occurred. Any molecular motion such as rotation, translation and desorption was not observed. Tunneling electron-induced reaction of the same molecule on the same substrate with a W tip was investigated. Three reactions of dissociation, rotation and desorption were found.

Publication list

1. Bo Yang, Emiko Kazuma, Yasuyuki Yokota, Yousoo Kim. Fabrication of sharp gold tips by a three-electrode electrochemical etching method with high controllability and reproducibility. *J. Phys. Chem. C* **2018**, *122*, 16950.
2. Rafael B. Jaculbia, Hiroshi Imada, Kuniyuki Miwa, Bo Yang, Emiko Kazuma, Norihiko Hayazawa, Yousoo Kim. Visualization of the resonance Raman effect from a

single molecule. (in submission)

3. Maria Vanessa C. Balois, Norihiko Hayazawa, Satoshi Yasuda, Katsuyoshi Ikeda, Bo Yang, Emiko Kazuma, Yasuyuki Yokota, Yousoo Kim, and Takuo Tanaka. Activation of forbidden phonon modes in defect-free graphene on Au(111) substrate by tip-enhanced nano confined light. *Proceedings of the Samahang Pisika ng Pilipinas.* SPP-2018-2B-03-1.

4. Chengxi Hu, Yuan Liu, Peng Liu, Bo Yang. Novel low loss, low permittivity (1-x)$Si0_2$ – $xTiO_2$ + ywt% H_3BO_3 microwave dielectric ceramics for LTCC applications. *Journal of alloys and compounds.* **2017**, *712*, 804.

5. Chengxi Hu, Yuan Liu, Wujun Wang, Bo Yang. Novel low permittivity $(Mg_{1-x}Cu_x)_2SiO_4$ Microwave dielectric ceramics. *Advances in Materials Science and Engineering.* **2018**, *10*, 1155.

Academic activities

[1] Dissociation of a single DMDS molecule on Au (111) surface. 11th RIKEN Summer School, Tsukuba, Japan, September 2016.

[2] 電気化学 STM と近接場分光の融合による電気化学探針増強ラマン分光装置の開発. 第 64 回応用物理学関係連合講演会、横浜、2017 年 3 月.

[3] 電気化学探針増強ラマン分光によるベンゼンチオール自己組織化膜の振動分光. 電気化学会第 84 回大会、八王子、2017 年 3 月.

[4] 電気化学探針増強ラマン分光による自己組織化単分子膜の局所振動分光. 2017 年真空・表面科学合同講演会、横浜、2017 年 8 月.

[5] Fabrication of sharp Au tips by three-electrode electrochemical etching. 12th RIKEN

Summer School, Chiba, Japan, September 2017.

[6] Local Vibrational Analysis of Benzenethiol Self-Assembled Monolayers on Au(111) Electrode using Electrochemical Tip-Enhanced Raman Spectroscopy. International Symposium on Surface Science, Tsukuba, Japan, October 2017.

[7] Development of Tip-Enhanced Raman Spectroscopy for Electrochemical Interfaces. The 5th Ito International Research Conference (IRRC-5), Tokyo, Japan, November 2017.

Acknowledgements

First of all, I'd like to express my sincere thanks to my supervisor Prof. Yousoo Kim. He gave me so many supports and encouragements in both my research work and daily life. I also specially acknowledge Dr. Emiko Kazuma and Dr. Yasuyuki Yokota for their kind help in my experiment. Many thanks to all the members in Surface and Interface Science Laboratory.

I thank the great support of RIKEN's International Program Associate (IPA). Acknowledgements to Graduate School of Science and Engineering of Saitama University in my course learning and daily affairs.

The research work was supported in part by Japanese Ministry of Education and Science, Grant-in-Aid for Young Scientists (B) [16K17862], RIKEN FY2015 Incentive Research Projects and RIKEN International Program Associate (IPA) program. We would also like to thank the Materials Characterization Support Unit of RIKEN in SEM measurements.